The Meteoritical Society

Meteoritics & Planetary Science 57, Nr 11, 2017–2041 (2022)
doi: 10.1111/maps.13917

Young magmatism and Si-rich melts on Mars as documented in the enriched gabbroic shergottite NWA 6963

Miles LINDNER [1]*, Dominik C. HEZEL [1,2], Axel GERDES[1,2], Horst R. MARSCHALL [1,2], and Frank E. BRENKER [1,3]

[1]Institut für Geowissenschaften, Goethe-Universität Frankfurt, Altenhöferallee 1, 60438 Frankfurt am Main, Germany
[2]Frankfurt Isotope and Element Research Center (FIERCE), Goethe Universität, 60438 Frankfurt am Main, Germany
[3]Hawai'i Institute of Geophysics and Planetology, University of Hawai'i at Mānoa, Honolulu, Hawaii 96822, USA
*Corresponding author. E-mail: mileslindner@stud.uni-frankfurt.de

(Received 14 March 2022; revision accepted 08 September 2022)

Abstract–Enriched shergottites contain interstitial Si-rich mesostasis; however, it is unclear whether such mesostasis is formed by impact or magmatic processes. We use laser ablation multicollector inductively coupled plasma mass spectrometry U–Pb measurements of minerals within the interstitial Si-rich mesostasis and of merrillite within the coarse-grained groundmass of Martian-enriched gabbroic shergottite Northwest Africa (NWA) 6963. The date derived of tranquillityite, Cl-apatite, baddeleyite, and feldspar from the Si-rich mesostasis is 172.4 ± 6.1 Ma, and the derived merrillite date is 178.3 ± 10.6 Ma. We conclude, based on textural observation, that merrillite is a late magmatic phase in NWA 6963, that it was not produced by shock, and that its U–Pb-system was not reset by shock. The indistinguishable dates of the gabbroic merrillite and the minerals within the Si-rich mesostasis in NWA 6963 indicate that the Si-rich mesostasis represents a late-stage differentiated melt produced in the final phase of the magmatic history of the gabbroic rock and not a shock melt. This can likely be transferred to similar Si-rich mesostases in other enriched shergottites and opens the possibility for investigations of Si-rich mesostasis in enriched shergottites to access their magmatic evolution. Our results also provide a crystallization age of 174 ± 6 Ma (weighted average) for NWA 6963.

INTRODUCTION

The suite of Martian meteorites allows detailed studies of Mars' geologic history and evolution. Today we have more than 300 meteorites from Mars in our collections, and radiometric dating showed that these cover almost the entire life span of Mars (e.g., Nyquist et al., 2001; Udry et al., 2020; Váci & Agee, 2020). Hence, Mars was and possibly is a geologically active planet, as also indicated by young lava flows (Hartmann et al., 1999) and seismic activity (Banerdt et al., 2020). The Martian meteorites represent a range of igneous rocks, such as highly pyroxene-rich rocks (e.g., nakhlites), dunites (chassignites), or have basaltic bulk compositions (e.g., shergottite meteorites). This range records information on magmatic processes in the Martian crust and mantle.

The youngest Martian meteorites and, hence, rock crystallization ages, are measured in the group of so-called enriched shergottites (see below), with ages ranging between approximately 225 and 165 Ma (Bellucci et al., 2018; Udry et al., 2020; Váci & Agee [2020] and references therein). Ages for all shergottites (including so-called intermediate and depleted shergottites) span a wider range; however, the majority of shergottites can still be regarded "young," with ages <600 Ma (Váci & Agee, 2020). Two exceptions exist with ages of 2.4 Ga (Herd et al., 2017; Lapen et al., 2017). The ages have been determined using either the Sm-Nd, Lu-Hf, or Rb-Sr radiogenic systems by measuring mineral separates and whole rock fractions (e.g., Borg et al., 2005; Combs et al., 2019; Ferdous et al., 2017; Marks et al., 2010; Shafer et al., 2010; Shih et al., 2009), or using the U–Pb radiogenic system and measuring Zr-rich accessory minerals or phosphates with in situ ion beam techniques (e.g., Koike et al., 2016; Moser et al., 2013; Staddon et al.,

2021; Wu et al., 2021; Zhou et al., 2013). Herd et al. (2007) used in situ laser ablation inductively coupled plasma mass spectrometry (LA-ICP-MS) U–Pb measurements of baddeleyite and generated data roughly in accordance with previously published young Sm-Nd and Rb-Sr ages (Borg et al., 2005). Two studies used in situ LA-ICP-MS U–Pb dating of the phosphate merrillite, demonstrating its potential applicability for age determinations in Martian meteorites (McFarlane & Spray, 2022; Wilson et al., 2019) using this technique–mineral combination.

Shergottites have picrite–basaltic or basaltic bulk compositions; however, enriched shergottites differ geochemically from intermediate and depleted shergottites by their relative enrichment in light rare earth elements (REEs) over heavy RREs. This enrichment is expressed in the $(La/Yb)_{CI}$-ratio, and shergottites with high ratios (>0.8) are designated enriched, those with low ratios (<0.3) depleted, and shergottites with $(La/Yb)_{CI}$ ratios between 0.3 and 0.8 are designated intermediate (Udry et al., 2020). This variation is believed to be inherited from the rock's mantle sources and is accompanied by systematic variations in the radiogenic isotope signatures for some of the incompatible elements. For example, enriched shergottites are characterized by relatively high initial $^{87}Sr/^{86}Sr$, but low initial $^{143}Nd/^{144}Nd$ and $^{176}Hf/^{177}Hf$ ratios, whereas depleted shergottites are characterized by relatively low initial $^{87}Sr/^{86}Sr$, and high initial $^{143}Nd/^{144}Nd$ and $^{176}Hf/^{177}Hf$ ratios. Based on the Lu/Hf isotope system, recent studies suggest that at least two enriched mantle sources for enriched shergottites exist, which, nonetheless, have similar crystallization and cosmic ray exposure ages (Combs et al., 2019). Similar variations between enriched and depleted shergottites are observed in other isotope systems—such as U–Pb and Re-Os (Udry et al., 2020).

A second classification scheme divides shergottites by their texture into four subgroups, which are (i) basaltic shergottites, (ii) olivine–phyric shergottites, (iii) poikilitic shergottites, and (iv) gabbroic shergottites (Udry et al., 2020). This last group of gabbroic shergottites is mineralogically similar to the first group, but coarse grained, which indicates a crystallization deeper within the Martian crust (Udry et al., 2020). Pyroxene and maskelynite are major components in all groups of shergottites, whereas olivine is present in olivine–phyric and poikilitic shergottites, and virtually absent in basaltic and gabbroic shergottites. Maskelynite in shergottites was produced by an isochemical conversion from plagioclase during shock. Minor mineral constituents are Fe-Ti oxides, iron sulfides, and the phosphates merrillite and apatite. An Si-rich glassy to cryptocrystalline mesostasis occurs interstitial to the larger grains (e.g., El Goresy et al., 2013; Herd et al., 2018; Sheen et al., 2021; Stolper & McSween, 1979) and is readily distinguished from the maskelynite by its texture and composition that is much higher in Si (>70 wt% SiO_2, i.e., granitic composition).

This minor, but common Si-rich mesostasis encapsulates trace minerals such as Zr-rich accessory phases, which are important constituents for U–Pb dating (Herd et al., 2018; Sheen et al., 2021); hence, Si-rich mesostasis is an important archive to determine shergottite chronology. Zr-rich phases previously used for U–Pb dating of Martian meteorites are baddeleyite and zircon (e.g., Moser et al., 2013). Tranquillityite with an ideal formula of $Fe^{2+}{}_8(Y,Zr)_2Ti_3Si_3O_{24}$ is another Zr-rich phase, but more commonly observed in lunar samples (Lovering et al., 1971). It has previously been described within enriched shergottite NWA 856, and there located within interstitial Si-rich mesostasis (Leroux & Cordier, 2006). The mineral was also reported for terrestrial samples from dolerite dykes and sills from Western Australia (Rasmussen et al., 2012), also located within late stage Si-rich interstices. For lunar and terrestrial samples, this mineral has successfully been used for Pb–Pb dating with ion probe techniques (e.g., Li et al., 2021; Rasmussen et al., 2008, 2012; Tartèse et al., 2013).

The phosphates merrillite and apatite are the major hosts of REE in shergottites (Shearer et al., 2015). Because the Sm-Nd radiogenic system has previously been used to derive shergottite crystallization ages (e.g., Marks et al., 2010; Shafer et al., 2010), phosphates are equally important components to reconstruct shergottite chronology. Recently, Wilson et al. (2019) and McFarlane and Spray (2022) showed the potential use of phosphates like merrillite and apatite for in situ U–Pb dating using LA-ICP-MS. This technique–mineral combination is promising, because merrillite, albeit modally a minor component, is widely present in shergottites with grain sizes that may range up to hundreds of μm (Shearer et al., 2015). Thus, no elaborate techniques are necessary for locating appropriate grains for measurements, as is the case for baddeleyite U–Pb dating (Herd et al., 2018). Additionally, LA-ICP-MS techniques require little sample preparation, compared to ion probe techniques. Merrillite has a chemical formula of $Ca_9Na(Mg,Fe)(PO_4)_7$. Typical merrillite found in Martian shergottites shows varying ferromerrillite ($Ca_9NaFe^{2+}[PO_4]_7$; Britvin et al., 2016), Ca-merrillite, and Na-merrillite endmember concentrations ($0.5 \times Ca^{2+} + 0.5 \times \square \leftrightarrow Na^{+}$; e.g., Shearer et al., 2015). Additionally, the incorporation of REE and Y via the coupled substitution $Ca + Na \leftrightarrow Y^{3+}, REE^{3+} + \square$ (Jolliff et al., 2006; Shearer et al., 2015) leads to an important REE-

merrillite ($REECa_8[Mg,Fe]\square[PO_4]_7$) endmember component. REE-rich merrillite is prevalent in lunar samples with up to 18 wt% $REE_2O_3 + Y_2O_3$ (Jolliff et al., 2006), while $REE_2O_3 + Y_2O_3$ in Martian merrillites are typically <1 wt% (Shearer et al., 2015). A solid solution between merrillite and whitlockite ($Ca_9[Fe,Mg][HPO_4][PO_4]_6$) has been observed for terrestrial samples, which can be described by a substitution of 0.5 × Ca ↔ H or Na ↔ H, for the Ca-merrillite endmember or the Na-merrillite endmember, respectively (Hughes et al., 2008). Merrillite in shergottites formed late during crystallization and occurs in various grain sizes from 10 to some few hundreds of μm (Shearer et al., 2015). It is often found in a textural relationship to apatite and it has been suggested that these associated apatites might be either a product of merrillite alteration, of magmatic origin, or both (Shearer et al., 2015; Słaby et al., 2017).

Si-rich mesostasis is most abundant in the enriched gabbroic shergottite Northwest Africa (NWA) 6963 (Filiberto et al., 2014; Gross & Filiberto, 2014) and primarily composed of <50 μm sized silica grains, intergrown with similarly sized K-rich feldspar and plagioclase laths, next to less abundant Fe-rich pyroxene, Fe-Ti oxides, phosphates, sulfide, and Zr-rich phases. We find that Zr-rich phases in NWA 6963 are mostly tranquillityite. A detailed description of Si-rich mesostasis in Shergotty and Zagami is provided by Stolper and McSween (1979). Such Si-rich mesostasis appears to be widespread in enriched shergottites, as it has been documented by, for example, Staddon et al. (2021) in NWA 7257 and NWA 8679 (their fig. 2a), Sheen et al. (2021) for several enriched shergottites (their figs. 4c, 5d, and 6d), Wu et al. (2021) in NWA 8653 (their fig. 1e), Zhou et al. (2013) in Zagami (their fig. 1i), He et al. (2015) in NWA 2975 and its pairings (their fig. 4a and 4b), and Leroux and Cordier (2006) in NWA 856 (their fig. 2) as well as El Goresy et al. (2013, their fig. 15b). To our knowledge, intermediate shergottites contain no Si-rich mesostasis, although NWA 13031 and NWA 13038 (listed as intermediate shergottites in Udry et al., 2020) contain silica (Gattacceca et al., 2021). Depleted shergottites contain similar components to the Si-rich mesostasis: A silica and K-Ba-rich melt + apatite is reported for Queen Alexandra Range (QUE) 94201 (McSween et al., 1996). Other workers (Harvey et al., 1996) report mesostasis that contain fayalite and SiO_2. Areas of mesostasis with "small blebs of K-feldspar and a silica phase" associated with phosphates, ulvöspinel, and ilmenite are reported for Dhofar 019 (Taylor et al., 2002). In Sayh al Uhaymir (SaU) 05, silica-rich melt inclusions are reported in olivine (Goodrich, 2003), but no mineral-interstices filling matter.

The origin and formation of the Si-rich mesostasis in enriched shergottites is disputed. Two entirely different processes have been proposed to explain its formation. The processes include (i) a late-stage crystallization product of relatively young mafic melts produced in the Martian crust and mantle (e.g., Filiberto et al., 2014; Herd et al., 2018; Stolper & McSween, 1979) and (ii) partial melting of the rock in response to an impact (El Goresy et al., 2013), likely the one that excavated the rock from Mars and sent it on its way to the Earth. Textural observations have been used to support each of the two propositions. Filiberto et al. (2014) stated that the texture is unlike textures of shock melts from shergottite Los Angeles, reported by Walton and Spray (2003). Filiberto et al. (2014) pointed out the resemblance of Si-rich mesostasis with graphic granite to suggest that the Si-rich mesostasis in NWA 6963 represents late-stage simultaneous crystallization of silica and alkali-feldspar. Stolper and McSween (1979) conclude the same for Si-rich mesostasis in Zagami and Shergotty, based on textural observations and the similar compositions of the Si-rich mesostasis and the eutectic compositions of the systems diopside–leucite–silica and diopside–nepheline–silica. El Goresy et al. (2013), however, suggest that the Si-rich mesostasis represents quenched melt of locally shock-molten plagioclase (labradorite). Deciding which of the two aforementioned scenarios is correct will provide the genetic context of the Si-rich mesostasis and then, potentially, allow for insights to the magmatic evolution of Mars.

Here, we study the origin of Si-rich mesostasis in the enriched gabbroic shergottite NWA 6963 by using in situ laser ablation multicollector inductively coupled plasma mass spectrometry (LA-MC-ICP-MS) U–Pb dating of minerals present within the Si-rich mesostasis —and compare their ages to groundmass merrillite ages, which we determined by the same technique. LA-MC-ICP-MS has so far only recently been used for U–Pb dating of merrillite in Martian meteorites (McFarlane & Spray, 2022; Wilson et al., 2019). Otherwise, ages for Martian meteorites were either determined using other isotopic chronometers and/or techniques (e.g., Borg et al., 2005; Combs et al., 2019; Ferdous et al., 2017; Koike et al., 2014, 2016; Marks et al., 2010; Moser et al., 2013; Shafer et al., 2010; Shih et al., 2009; Terada et al., 2003; Wu et al., 2021; Zhou et al., 2013), or the same isotopic chronometer and technique, but used on a different phase than merrillite, for example, baddeleyite in basaltic Martian meteorites (Herd et al., 2007, 2018; Sheen et al., 2021). Merrillite is a minor but ubiquitous phase in NWA 6963, and part of the coarse-grained groundmass with grain sizes of 100–1000 μm. As we will show, it was most likely not produced by shock but is a primary component of the rock. Hence,

similar ages of minerals in the Si-rich mesostasis and the groundmass merrillite would point to a formation of both during magmatic crystallization of the rock, while different ages would be best interpreted as two different events, thereby not excluding a shock origin of the Si-rich mesostasis. The U–Pb data can be further used to determine a crystallization age for NWA 6963, which to our knowledge has not been reported before. We will also characterize the mineral tranquillityite in the Si-rich mesostasis of NWA 6963, as only a single study so far reports its occurrence within a Martian meteorite (Leroux & Cordier, 2006).

METHODS

All analyses were performed in the laboratories of the Department of Geoscience, University Frankfurt.

Sample Documentation with Reflected Light Microscopy

Detailed images covering the whole sample surface were obtained before and after LA-MC-ICP-MS measurements using a Keyence VHX 6000 digital optical microscope in nonpolarized coaxial epi-illumination and in nonpolarized non-coaxial epi-illumination ("ring-light").

Sample Documentation and Qualitative EDX Analyses Using SEM

The sample was cleaned and carbon coated. A JEOL JSM-6490 scanning electron microscope (SEM) was used for sample documentation before LA-MC-ICP-MS and electron probe microanalyzer (EPMA) measurements. Qualitative analyses were performed with an Oxford Instruments energy-dispersive X-ray (EDX) system, attached to the SEM, using an acceleration voltage of 15 kV. X-ray intensities were calibrated every hour on a pure cobalt reference. Data were processed with the Oxford Instruments Inca software.

U–Pb Dating of Merrillite and Mesostasis Minerals Using LA-MC-ICP-MS

Isotope analyses were performed in a single session using a Thermo Scientific Neptune Plus multicollector ICP-MS, coupled to a RESOlution 193 nm ArF Excimer (CompexPro 102, Coherent) laser ablation system equipped with an S-155 two-volume ablation cell (Laurin Technic, Australia). The settings of the laser and the ICP-MS instrument as well as information on the data processing are given in Table S1 in supporting information. Prior to the measurements, the plasma was tuned for low oxide formation rate, with reference material ablation and monitoring UO_2. The laser ablation system was equipped with an adjustable aperture. For measurements of tranquillityite grains with high length to width ratio, a rectangular aperture was used, resulting in a spot of 12 μm × 35 μm. This geometry was also used for the reference materials and merrillite measurements. Reference materials (Table S2 in supporting information) were NIST SRM-614, USGS basaltic glass GSC-G, Durango apatite, Mudtank zircon, and Diamantina apatite (Minas Gerais). U/Pb fractionation and machine drift of all analyses were corrected using NIST SRM 614. In order for the ages of the Mudtank zircon and Durango apatite to match the literature values (Gain et al., 2019; Paul et al., 2021), the $^{206}Pb/^{238}U$ ratios must be corrected down by 5% and 3.3%, respectively (see supplementary discussion). Tranquillityite and baddeleyite were corrected like the Mudtank zircon, while for Cl-apatite and merrillite measurements, the Durango apatite correction factor was applied. Mesostasis feldspar was not corrected, relative to the NIST SRM 614 reference. All measurement conditions are listed in Table S1. Prior to the measurements, any carbon coating of a sample was removed by short polishing of the sample surface with diamond paste and subsequent rinsing with ethanol. A pre-ablation was performed before each spot, to remove any remaining sample contamination. The data are plotted in a Tera–Wasserburg diagram without any correction for initial $^{207}Pb/^{206}Pb$. Within Tera–Wasserburg space, data points from minerals with common crystallization age, that crystallized from the same source and did not suffer modification of U and Pb, are represented as mixture of a theoretical pure radiogenic endmember and an endmember containing no radiogenic lead produced by the decay of U since their crystallization (e.g., Ludwig, 1998). Endmember values can be derived by the intercept of the regression through the data points with the ordinate and the concordia line, respectively. If above conditions are true, these values represent the initial $^{207}Pb/^{206}Pb$ composition of the sample and crystallization age (Ludwig, 1998) of the dated phases.

For most of the minerals sampled with LA-MC-ICP-MS, we used correction factors to correct for elemental fractionation, relative to the calibration with the NIST SRM 614 reference. Because no mineral matrix matched references were available to us for most sampled minerals, except for mesostasis Cl-apatite, these correction factors are derived from nonmineral matrix matched references available (i.e., Durango apatite and Mudtank zircon for merrillite and tranquillityite/baddeleyite, respectively). This might introduce systematic error. We used a constant correction of −3.3% relative to the NIST SRM 614 on the measured $^{206}Pb/^{238}U$ ratio, appropriate for, and derived from,

Durango apatite for merrillite measurements. Using apatite for correcting merrillite with LA-ICP-MS has been done before (McFarlane & Spray, 2022) and yielded reasonable results. As phosphates differ in their structure from the silicate glass NIST SRM 614 reference, we consider this correction favorable over no correction. This approach is supported by the results of our merrillite U–Pb measurements. The derived values for intercept date and initial Pb are within the literature values for enriched shergottites, measured using other isotope systems or high precision Pb isotope measurements, respectively (Bellucci et al., 2015; Borg et al., 2005; Bouvier et al., 2005, 2008, 2009; Nyquist et al., 2001; Udry et al., 2020; Váci & Agee, 2020). They are also in accordance with a recent study that used LA-quadrupole-ICP-MS on merrillite grains of enriched shergottite Los Angeles (McFarlane & Spray, 2022). Thus, we consider our approach for merrillite U–Pb measurements justified and the results robust. We like to emphasize that a merrillite matrix matched reference material would be most beneficial for future LA-ICP-MS studies using the U–Pb system and merrillite, also in view of future returned samples.

Nonmineral matrix matched references were used for the correction of U–Pb measurements of minerals in the Si-rich mesostasis. Here, especially tranquillityite and baddeleyite data were treated, using a constant −5% correction relative to the NIST SRM 614 on the measured $^{206}Pb/^{238}U$ ratio, appropriate for, and derived from, the Mudtank zircon reference. We consider this correction favorable over no correction, as baddeleyite and tranquillityite mineral matrices should be much more similar to zircon than to a silicate glass matrix. The Si-rich mesostasis feldspar spots were not corrected for elemental fractionation, relative to the NIST SRM 614 reference. It is suggested that feldspar within Si-rich mesostasis in NWA 6963 is amorphous (Hamilton & Filiberto, 2015), and thus very similar to the NIST SRM 614 alkali–silicate glass reference material, which justifies this approach. The NIST SRM 610 alkali–silicate glass reference has been used before for correction of U–Pb measurements of K-rich diaplectic glass within Los Angeles (McFarlane & Spray, 2022). A relatively simple approach would be to introduce an uncertainty on this constant correction. An older intercept date would be the result for the Si-rich mesostasis U–Pb measurement (and no significant change is observed for the merrillite U–Pb measurement), if an additional uncertainty is introduced on the constant correction relative to the NIST SRM 614 and propagated with the squared sums of the relative errors onto the uncertainty of the $^{238}U/^{206}Pb$ value. However, it is not possible to estimate realistic values for this uncertainty on the correction and the mean squared weighted deviation (MSWD) value would decrease to a lower number, suggesting that errors then are strongly overestimated.

Furthermore, the U–Pb measurements of minerals in the Si-rich mesostasis are mixtures of different phases with different elemental fractionation. Consequently, applying a constant correction of, for example, −5% on the measured $^{206}Pb/^{238}U$ ratio (methods) of spots containing not purely tranquillityite but in fact tranquillityite and some other phases (most likely feldspar and silica as those are the dominant phases) may generate a systematic error. We discuss this error in a supplementary discussion and show that, instead of a constant correction, using a weighted mean correction factor for tranquillityite spots, which is weighted by the volume fractions of minerals sampled, would lead to a derived intercept date of 176.8 ± 6.1 Ma (2σ, MSWD = 0.62, n = 30). This date is older by 4.4 Ma than the date derived using a constant correction derived from zircon. Combined with the observation that an uncertainty on a constant correction would also lead to older intercept dates, we thus report here our original date of 172.4 ± 6.1 Ma for the crystallization age of the Si-rich mesostasis. We note that this result is best interpreted as a minimum age, with the "true" value lying most likely within the upper uncertainty range and possibly is an age of as high as 176.8 ± 6.1 Ma.

Finally, based on our data, it appears that terrestrial Pb has no significant influence on our measurements. Our derived initial $^{207}Pb/^{206}Pb$ values for merrillite and Si-rich mesostasis are 0.9816 ± 0.0067 and 0.9766 ± 0.0028 (2σ), respectively. They are in accordance with and fall within the upper range of previously reported values for enriched shergottites (Bellucci et al., 2015; Borg et al., 2005; Bouvier et al., 2005, 2008, 2009; McFarlane & Spray, 2022). Contamination with modern terrestrial Pb with a $^{207}Pb/^{206}Pb$ ratio of approximately 0.84 (Stacey & Kramers, 1975) would have shifted the $^{207}Pb/^{206}Pb$ ratios to lower values. An explanation for the insignificant amount of contamination is the precautionary pre-ablation before each measurement to remove surficial contamination. Also, the Si-mesostasis-rich areas within NWA 6963 are not heavily fractured and thus are less susceptible to contamination by terrestrial weathering. For heavily fractured merrillite, the small spot size and elongated shape allowed for largely avoiding fractures or only sampling small volumes of these, and thus largely avoiding possible contamination caused by terrestrial weathering.

Determining Mineral Compositions Using EPMA

The JEOL Hyperprobe JXA-8530F Plus field emission electron microprobe was used for qualitative

combined wavelength-dispersive X-ray spectrometry (WDS) and EDX mapping and quantitative wavelength-dispersive X-ray analysis (WDX) element analysis after LA-MC-ICP-MS measurements. Each sample was cleaned in an ultrasonic bath for 15 min using petrol-ether, dried in a vacuum oven, and then carbon coated. Mesostasis grains (tranquillityite, baddeleyite, and feldspar; smaller than 20 μm in at least one dimension) were measured with an acceleration voltage of 10 kV and larger groundmass grains (merrillite) with 15 kV. The beam current was set to 20 nA. A focused spot (<100 nm) was used for tranquillityite and baddeleyite and a defocused, 8 μm diameter, circular spot for feldspar to prevent Na loss. Because for accurate analysis of Cl- and F-apatite another different WDX measurement protocol would have been necessary (Goldoff et al., 2012), mesostasis and groundmass apatite was mainly measured and characterized qualitatively using the EDX. Merrillites were measured next to the U–Pb laser ablation spots using spot sizes between 1 and 10 μm. The merrillite totals increase slightly when spot sizes increase from 4 to 10 μm, mainly due to an increase in measured P_2O_5 concentration. The built-in CITZAF matrix correction was used for quantification. Crystal positions and measurement times for the analyzed elements are listed in Tables S3 and S4 in supporting information.

Raman Spectrometry

We used a Witec α 300r Raman system equipped with a 532 nm laser to confirm selected mineralogies. A 1800 L mm^{-1} grating was used to receive a spectral resolution of 1–2 cm^{-1} in the range of 100–1200 wave numbers. For the small tranquillityite grains, a 100× Zeiss EC Epiplan objective was used yielding a spot size of 1–2 μm, and for the larger merrillite grains, a 50× Zeiss EC Epiplan objective was used, yielding a spot size of 3–4 μm. The laser power had to be kept low (2.5 mW) for tranquillityite measurements, as oxidation occurred at high power (i.e., a black spot at ≥10.0 mW laser output at 100× magnification). Total measurement lifetimes were ≤20 s. Spectra were visualized using the "Crystal Sleuth" software from the RRUFF project (Lafuente et al., 2016). The "remove background" function was used if a background correction was necessary. Peak positions were determined manually in the spectrum viewer.

RESULTS

Petrography and Structure of NWA 6963

The sample is a polished thick section of the enriched gabbroic shergottite NWA 6963 (Fig. 1). Filiberto et al. (2014, 2018) provide a detailed textural and mineralogical description, in which they classify NWA 6963 as an enriched gabbroic shergottite due to its coarse-grained minerals, indicating an intrusive origin. Major groundmass phases are large pyroxene grains (up to >1 mm) and maskelynite. Minor groundmass components are merrillite and apatite (Selin et al., 2014), Fe-Ti oxides (at least two different Fe-Ti-oxides are present, based on backscatter electron [BSE] images). These are either intergrown or present within the other along fractures) and sulfide. All coarse-grained phases, except maskelynite, are heavily fractured, in response to a shock event. Considerable amounts of Si-rich mesostasis occur as glassy to fine-crystalline material interstitial to the larger minerals (Gross & Filiberto, 2014). The modal abundance of confirmed Si-rich mesostasis (i.e., Si-rich mesostasis documented in this study with either SEM or reflected light microscopy) in our sample is approximately 1.5%. This is a minimum estimation, as likely not all Si-rich mesostasis areas are documented. For comparison, the entry for NWA 6963 in the Meteoritical Bulletin reports a modal abundance of 2% (Ruzicka et al., 2014). U–Pb ages were determined in the coarse-grained merrillites as well as in the four accessory phases tranquillityite, baddeleyite, Cl-apatite, and feldspar, which all occur in the Si-rich mesostasis. In the following, we first describe the merrillite and then the accessory minerals in the Si-rich mesostasis.

Petrography and Petrology of Minerals Used for U–Pb Dating

Coarse-Grained Groundmass Merrillite

The phosphates merrillite and apatite (Fig. 2) are minor constituents of the coarse-grained NWA 6963 groundmass, consistent with previous studies (Filiberto et al., 2014, 2018; Selin et al., 2014; Wilson et al., 2012). We confirmed merrillite—rather than whitlockite—by significant Na concentrations (Table 1) as well as the absence of an HPO_4^{2-} related peak in its Raman spectrum (Jolliff et al., 2006; Shearer et al., 2015). Merrillite is observed with or without apatite intergrowths and rims (Fig. 2a–d; Fig. S1 in supporting information). This is best seen in contrast-enhanced SEM images (Fig. 2d) using Fiji software (Schindelin et al., 2012). We identified Cl-rich as well as Cl- and F-rich apatite within merrillite grains, based on qualitative EDX measurements (cf. Selin et al., 2014). Merrillite grains show a wide variability of shapes from anhedral to lath shaped, to subhedral, to euhedral. Subhedral to euhedral grains that are cut approximately parallel to their *c*-axis have length-to-width dimensions of 250–1000 μm by 40–140 μm. Anhedral grains are smaller

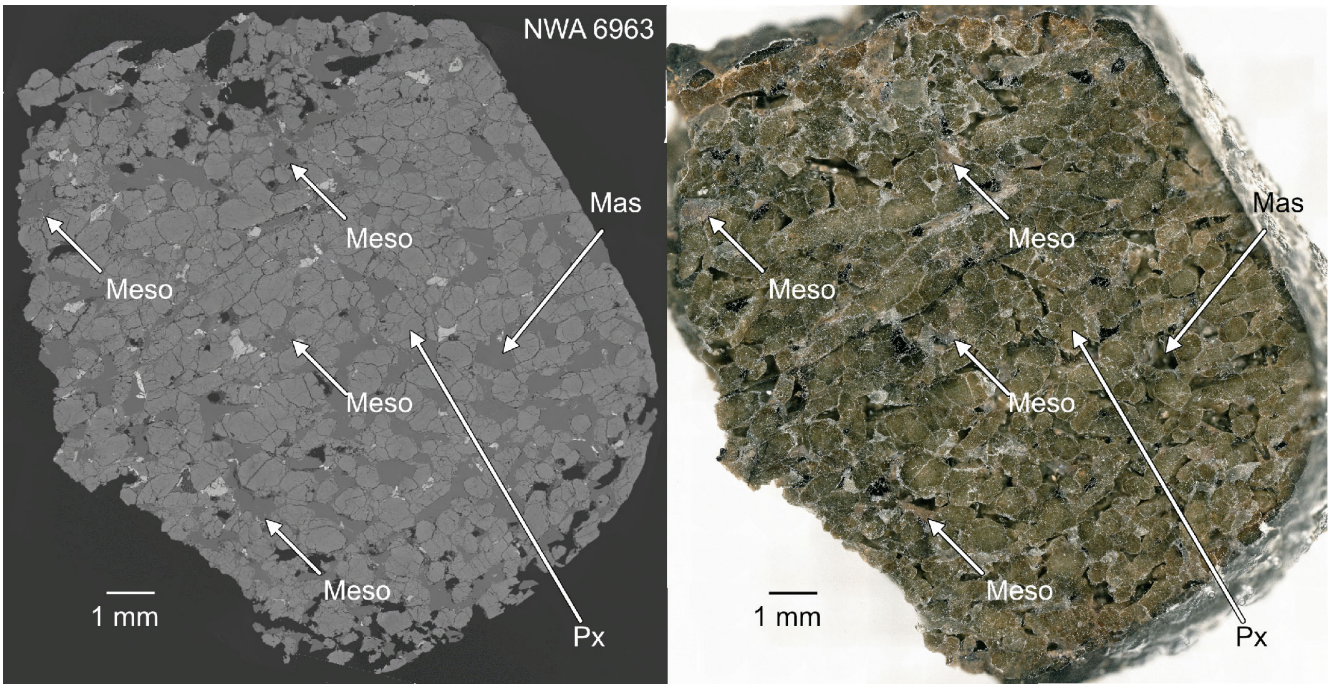

Fig. 1. Left: Stitched backscatter electron (BSE) image. Right: stitched nonpolarized, non-coaxial reflected light microscopy image. Arrows point to Si-rich mesostasis areas (Meso), maskelynite (Mas), and pyroxene (Px). (Color figure can be viewed at wileyonlinelibrary.com.)

with length-to-width dimensions of up to 230 μm × 750 μm. The merrillite grains contain melt inclusions appearing either as small, circular inclusions in the center of the grains with 1–11 μm in diameter and aligned in linear arrays parallel to the long axis—or as larger, either circular (up to 30 μm in diameter) or elongated (up to 120 μm in length) melt inclusions (Fig. 2c). The melt inclusions have feldspathic or Fe-rich pyroxene-like compositions. Additional small Fe-Ti oxide or iron sulfide inclusions occur.

Representative EPMA measurements are shown in Table 1 together with values from Filiberto et al. (2018). Measurements with totals lower than 98 wt% were excluded in Table 1 and for average formula and Mg# calculations. However, all measurements (the minimum of the totals is 97.7 wt%) are given in the supporting information. Merrillites have low compositional variability with an average composition of $Ca_{18.31(0.32)}Mg_{1.06(0.21)}Fe_{1.07(0.22)}Na_{1.06(0.27)}(P_{1.00(0.01)}O_4)_{14}$ (numbers in parentheses show 3σ standard deviation from the average). The major element composition indicates a comparatively high ferromerrillite component (Britvin et al., 2016), thereby being different to the results reported by Filiberto et al. (2018): We find an Mg# of 50 (±10; 3σ standard deviation of 26 individual analyses on 17 individual grains), while the average Mg# of analyses reported by Filiberto et al. (2018) is 75 (±3; 3σ standard deviation of the four published analyses). The Mg# is, however, in agreement with other measurements of merrillite in enriched shergottites (Shearer et al., 2015; Ward et al., 2017). Further deviations to published values by Filiberto et al. (2018) are higher SiO_2, Na_2O, and MnO concentrations, the latter in accordance with higher FeO values (Shearer et al., 2015).

By using Raman spectrometry on 5 of 11 grains that were used for U–Pb dating, we additionally confirmed merrillite for these grains. A representative spectrum is shown in Fig. 3. The spectra closely resemble merrillite spectra from shergottites EETA79001, Los Angeles (Wang et al., 2004; Wilson et al., 2019), and the L6 chondrites Suizhou and Sixiangkou (Chen et al., 1995; Xie et al., 2002, 2015). Compared to the reference spectrum (Suizhou L6 chondrite, Xie et al., 2015), the doublet at 958 and 973.5 cm^{-1} is slightly less well resolved and shifted about 2.5 cm^{-1} toward lower wave numbers. The somewhat broader doublet peaks may be a result of peak-broadening due to reduced crystallinity resulting from the shock event, or due to the incorporation of REE and Y (Jolliff et al., 2006; Shearer et al., 2015). The latter might be supported by significant concentrations of Y and Ce (Table 1). An additional peak not observed in the reference spectrum is visible at 1099.2 cm^{-1}. A peak at 923 cm^{-1} that is typically associated with HPO_4^{2-} groups is absent, thus

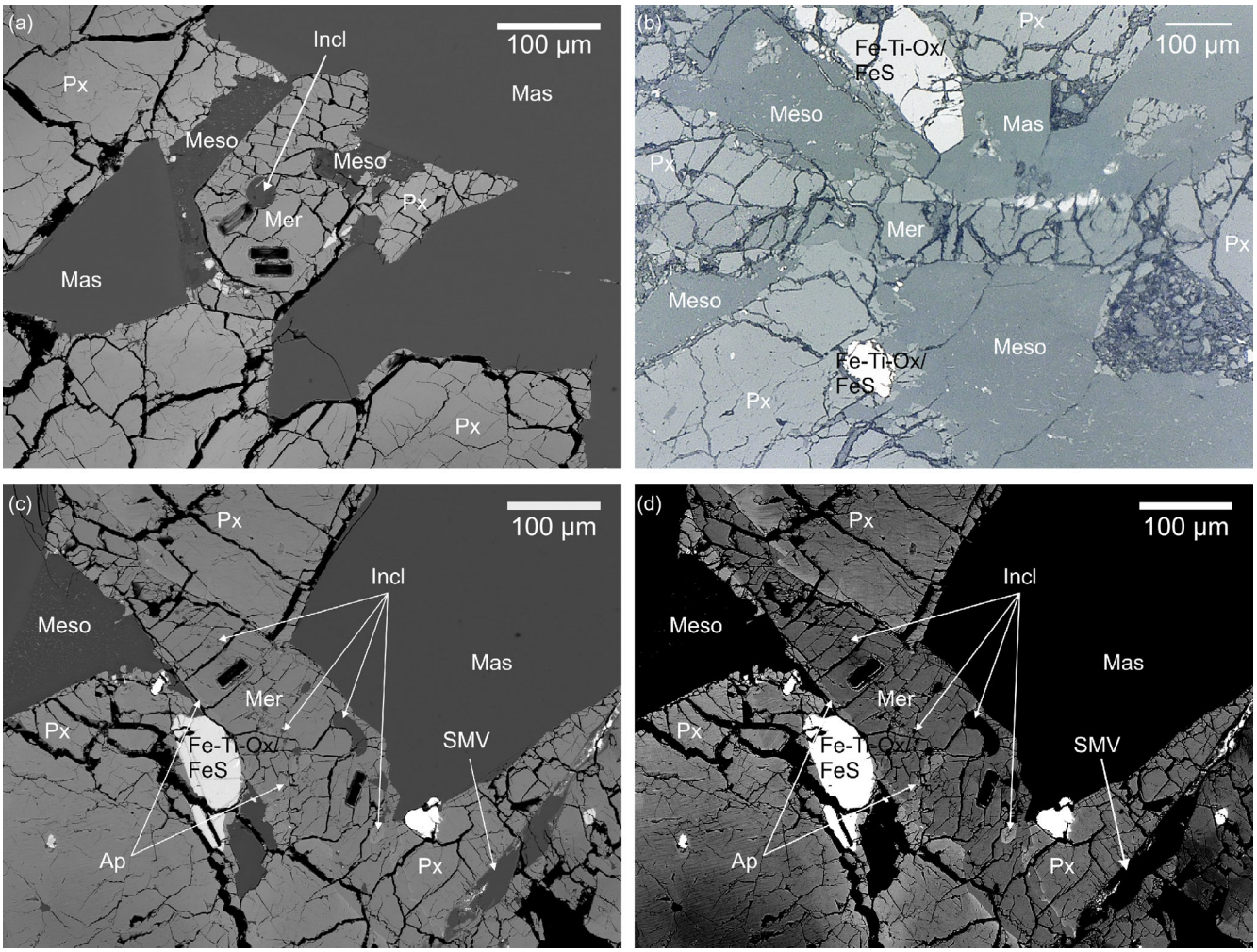

Fig. 2. Appearances of merrillite in NWA 6963. a) BSE image of a euhedral merrillite grain cut nearly perpendicular to the *c*-axis, next to maskelynite, clinopyroxene, and small areas of Si-rich mesostasis, and containing a circular melt inclusion. Rectangular, black ablation spots of U–Pb measurements are also visible in the merrillite grain. b) Reflected light image with coaxial illumination of a euhedral merrillite grain next to clinopyroxene, Fe-Ti oxide or iron sulfide, mesostasis areas, and maskelynite. c, d) BSE images of the same merrillite grain (GGMer4), but different contrast settings. The grain contains a trail of small circular, dark-gray melt inclusions and larger dark-gray and light-gray melt inclusions and is in contact to a shock melt vein. The apatite is only visible in the high contrast image (d) within and at the rim of the merrillite grain. Similarly, a melt inclusion with pyroxenic melt composition is better visible in (d). Px = pyroxene; Mas = maskelynite; Mer = merrillite; Incl = melt inclusion; Ap = apatite; Meso = Si-rich mesostasis area; Fe-Ti-Ox/FeS = Fe-Ti oxide or iron sulfide; SMV = shock melt vein. (Color figure can be viewed at wileyonlinelibrary.com.)

confirming merrillite and excluding whitlockite (Jolliff et al., 2006; Shearer et al., 2015). The measured Raman spectra also exclude tuite, the high-pressure polymorph of merrillite and apatite, as the present phase (Xie et al., 2002, 2004, 2013) at the locations of Raman point measurements.

The Accessory Minerals Tranquillityite, Cl-Apatite, Baddeleyite, as Well as Feldspar in the Si-Rich Mesostasis

The fine-grained, Si-rich mesostasis is typically located interstitial to the groundmass minerals clinopyroxene, merrillite, Fe-Ti oxide/sulfide, as well as maskelynite (Fig. 4a–c). Merrillite was observed close to (within 50 µm), or in contact with Si-rich mesostasis in 20 of 31 cases, despite merrillite being a minor phase in NWA 6963 (Filiberto et al., 2014, 2018; Wilson et al., 2012). Similarly, Fe-Ti oxides or iron sulfides—also minor phases (Filiberto et al., 2014, 2018; Wilson et al., 2012)—are often close to (within 50 µm), or in contact with Si-rich mesostasis (18 of 31 occurrences). The sizes of the Si-rich mesostasis areas are highly variable, ranging from approximately 30 µm × 60 µm to approximately 840 µm × 360 µm. It mainly consists of

Table 1. Representative EPMA WDS (wt%) analyses of merrillite in NWA 6963 and published values.

Spot size (μm)	4	4	4	4	4	4	4	10	10	Filiberto et al. (2018)			
SiO_2	0.09	0.08	0.10	0.07	0.10	0.17	0.08	0.07	0.07	0.32	0.36	0.34	0.32
TiO_2	<0.03	<0.03	<0.03	<0.03	<0.03	<0.03	<0.03	<0.03	<0.03	0.02	0.01	0.03	b.d.
Al_2O_3	<0.03	<0.03	<0.03	0.03	<0.03	<0.03	<0.03	<0.03	<0.03	n.a.	n.a.	n.a.	n.a.
Cr_2O_3	<0.06	<0.06	<0.06	<0.06	<0.06	<0.06	<0.06	<0.06	<0.06	n.a.	n.a.	n.a.	n.a.
MgO	1.87	1.82	1.96	2.12	1.81	1.82	2.16	2.05	1.92	3.23	3.21	3.30	3.11
FeO	3.60	3.63	3.39	3.30	3.97	3.74	3.04	3.32	3.46	1.86	1.99	1.80	1.90
MnO	0.15	0.16	0.19	0.17	0.18	0.16	0.14	0.16	0.14	0.07	0.09	0.11	0.06
CaO	47.11	47.01	46.54	46.23	46.47	46.07	46.38	46.34	46.65	47.9	47.74	47.14	47.34
Na_2O	1.38	1.40	1.36	1.56	1.38	1.69	1.57	1.49	1.34	1.28	1.27	1.36	1.24
K_2O	0.05	0.05	0.06	0.05	0.05	0.12	0.07	0.07	0.05	n.a.	n.a.	n.a.	n.a.
P_2O_5	45.61	45.26	44.57	45.07	44.51	44.41	44.59	45.04	44.76	45.86	45.03	44.08	44.8
Y	0.13	0.13	0.11	0.11	0.12	0.12	0.12	0.13	0.13	n.a.	n.a.	n.a.	n.a.
Ce	0.08	0.06	0.04	0.05	0.05	0.03	0.04	0.06	0.04	n.a.	n.a.	n.a.	n.a.
Total[a]	100.12	99.64	98.35	98.81	98.68	98.37	98.23	98.77	98.62	100.54	99.69	98.16	98.78
Number of cations calculated on a basis of 56 O per formula unit													
Si	0.033	0.029	0.037	0.026	0.037	0.063	0.030	0.026	0.026	0.110	0.130	0.130	0.120
Ti	b.d.	b.d.	b.d.	b.d.	b.d.	b.d.	b.d.	b.d.	b.d.	0.010	0	0.010	n.a.
Al	b.d.	b.d.	b.d.	0.013	b.d.	b.d.	b.d.	b.d.	b.d.	n.a.	n.a.	n.a.	n.a.
Mg	1.009	0.988	1.078	1.158	0.995	1.003	1.188	1.120	1.053	1.720	1.730	1.800	1.680
Fe^{2+}	1.089	1.105	1.045	1.010	1.223	1.155	0.937	1.017	1.064	0.550	0.600	0.550	0.580
Mn	0.046	0.049	0.059	0.053	0.056	0.050	0.044	0.050	0.044	0.020	0.030	0.030	0.020
Ca	18.276	18.345	18.395	18.146	18.358	18.243	18.330	18.204	18.388	18.310	18.470	18.520	18.460
Na	0.969	0.989	0.973	1.108	0.987	1.211	1.123	1.059	0.956	0.890	0.890	0.960	0.880
K	0.023	0.023	0.028	0.023	0.024	0.057	0.033	0.033	0.023	n.a.	n.a.	n.a.	n.a.
P	13.980	13.955	13.919	13.978	13.893	13.895	13.924	13.980	13.940	13.850	13.770	13.680	13.800
Y	0.033	0.031	0.027	0.027	0.029	0.030	0.029	0.031	0.033	n.a.	n.a.	n.a.	n.a.
Ce	0.012	0.009	0.007	0.008	0.008	0.005	0.007	0.009	0.007	n.a.	n.a.	n.a.	n.a.
$\Sigma_{Cations}$	35.470	35.524	35.568	35.549	35.610	35.711	35.644	35.530	35.534	35.470	35.610	35.690	35.540
Mg#	48.1	47.2	50.8	53.4	44.8	46.5	55.9	52.4	49.7	75.8	74.2	76.6	74.3

n.a. = not analyzed/not given; b.d. = below detection limit.
[a]Totals are based on all elements as oxides.

silica and feldspar intergrowths with a slight feldspar predominance. Texturally, Si-rich mesostasis in NWA 6963 is different from shock melt pockets as described for the enriched basaltic shergottite Los Angeles (Walton & Spray, 2003) and intermediate shergottites (Walton & Herd, 2007; Walton et al., 2012), in accordance with observations of Filiberto et al. (2014). Feldspar within NWA 6963 Si-rich mesostasis typically occurs as needle-like grains. Fourier transform infrared (FT-IR) measurements on Si-mesostasis areas suggest that silica and feldspar grains might be amorphous rather than crystalline as a result of shock (Hamilton & Filiberto, 2015). To avoid confusion with coarse-grained amorphous maskelynite, we will still use the word feldspar for this fine-grained mesostasis-phase throughout the text. Our EPMA analysis on larger feldspar grains within Si-rich mesostasis (>8 μm due to the defocused spot size) give compositions of $An_{32-36}Ab_{59-62}Or_{3-10}$. One grain shows a more K-rich composition of $An_{28}Ab_{49}Or_{23}$. We note that the larger grains might not be representative for most of the feldspar in Si-rich mesostasis as these are typically smaller.

The accessory phases tranquillityite, Cl-apatite, Fe-rich pyroxene, Fe-Ti oxide, iron sulfide, and baddeleyite are embedded in the silica–feldspar intergrowth. Fe-rich pyroxene, Fe-Ti oxide, or iron sulfide have grain sizes of up to 100 μm in the longest dimension; however, smaller grains <30 μm are much more common. These three minerals are not considered further, as we did not use these for U–Pb age determinations.

Tranquillityite is a rare mineral that might be confused with other Zr-containing minerals. It has been described as zircon in NWA 6963 previously (Filiberto et al., 2014) and is not usually found within Martian meteorites or reported for Martian meteorites, except for NWA 856 (Leroux & Cordier, 2006). We therefore studied tranquillityite in more detail. Individual grains are approximately 5–35 μm in length and <1 μm up to 5 μm in width, although their widths rarely exceed 2 μm. BSE images show that the bright and mostly euhedral tranquillityite grains with acicular shapes

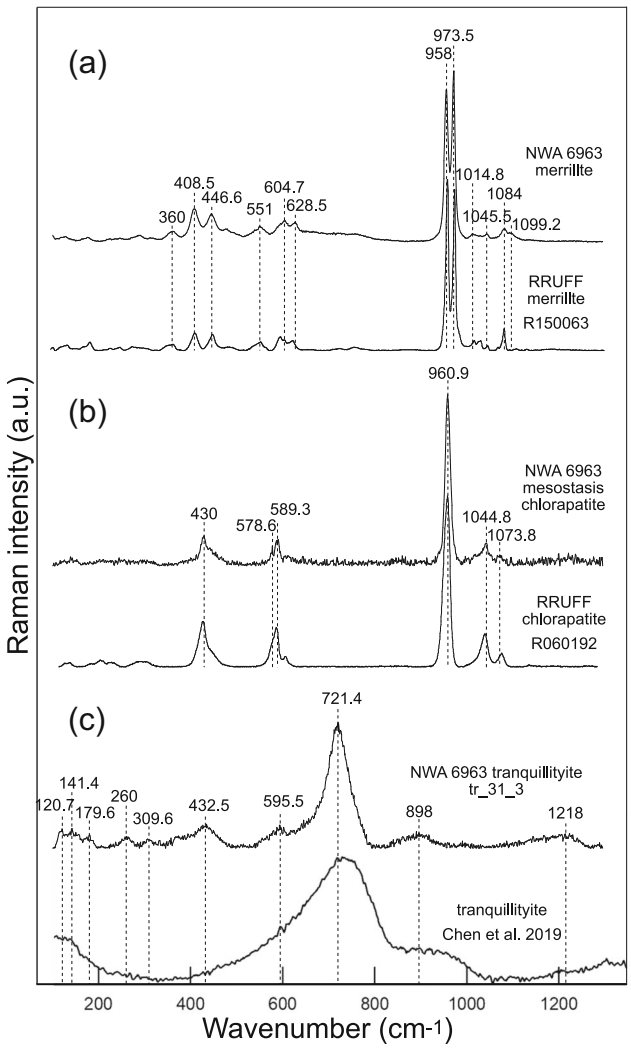

Fig. 3. Raman spectrum of merrillite, mesostasis Cl-apatite, and mesostasis tranquillityite in NWA 6963. a) Merrillite Raman spectra: The upper spectrum is from this study, the lower is from the RRUFF database (Lafuente et al., 2016). b) Cl-apatite Raman spectra: The upper spectrum shows a measurement on a mesostasis Cl-apatite grain. A background subtraction has been applied. The spectrum matches well the reference spectrum (lower spectrum) for Cl-apatite from the RRUFF database (Lafuente et al., 2016). c) Tranquillityite Raman spectra: The upper spectrum is measured on grain tr_31_3 and is representative for other tranquillityite spectra. A background subtraction has been applied. The lower spectrum is from a lunar tranquillityite from Chen et al. (2019) for comparison.

are strongly fractured (Fig. 4d). The abundance of tranquillityite is variable with either numerous grains distributed throughout the Si-rich mesostasis or with only a small number of grains present. Qualitative EDX spectra of pure tranquillityite are difficult to obtain and mostly overlain by element peaks from surrounding phases (a representative spectrum is shown in Fig. 5). Similarly, quantitative EPMA analysis is often mix-analyses. Pure tranquillityite analysis often has totals <100 wt%, because of fractures, and elements not measured, such as Hf or Nb. Results of EPMA measurements are listed in Table 2, while literature values of EPMA measurements of lunar and terrestrial tranquillityites, and one TEM EDX derived composition for Martian tranquillityite are listed in Table 3. For Table 2, calculated average tranquillityite composition and further comparison with literature values, only measurements without a strong indication of mix-analysis and with totals >98 wt% were considered. NWA 6963 tranquillityite composition differs from lunar and terrestrial tranquillityite (Fig. S2 in supporting information). Literature data of lunar tranquillityite have lower MgO and MnO concentrations than the tranquillityite measured here. SiO_2 and FeO concentrations of lunar tranquillityite are also lower; however they show some overlap with NWA 6963 tranquillityite. CaO and ZrO_2 concentrations are mostly higher in lunar tranquillityite, while TiO_2 and Al_2O_3 are similar. Tranquillityite in Si-rich mesostasis in the basaltic shergottite NWA 856 (Leroux & Cordier, 2006) has very similar compositions to the tranquillityite we measured, albeit with relatively high ZrO_2 and lower CaO and concentrations. Leroux and Cordier (2006) notice the absence of Y in NWA 856 tranquillityite compared to Y-rich lunar tranquillityites, and Y is also below the detection limit in our measurements (<approximately 0.1 wt% Y_2O_3). Compositions of terrestrial tranquillityite from dolerite sills in Western Australia (Rasmussen et al., 2012) are higher in TiO_2 and CaO, mostly lower in ZrO_2 and Al_2O_3, and overlap in SiO_2, MnO, MgO, and FeO. A further difference are the significant Y_2O_3 concentrations in terrestrial tranquillityite (Rasmussen et al., 2012).

We derive the tranquillityite formula as follows: $Fe_{7.61(0.70)}Mg_{0.44(0.14)}Ca_{0.20(0.06)}Ti_{2.96(0.60)}Zr_{1.17(0.30)}Al_{0.24(0.21)}Si_{3.48(0.81)}O_{24}$ (values in parentheses show the 3σ standard deviation from the average). The average cation total is 16.24 atoms per formula unit (apfu) instead of 16 and differs significantly from the first published formula (Lovering et al., 1971). There is excess Si in all our compositions, and five of nine show additional excess in Ti. Zr shows a deficit, while Y is absent. If all Fe is ferrous, the sum of divalent cations exceeds 8 apfu in eight of nine cases. Differing compositions from the original formula are also observed for the reported terrestrial tranquillityite compositions and tranquillityite compositions from shergottite NWA 856, as well as for lunar tranquillityite from northern Oceanus Procellarum (Table 3) (Leroux & Cordier, 2006; Li et al., 2021; Rasmussen et al., 2012).

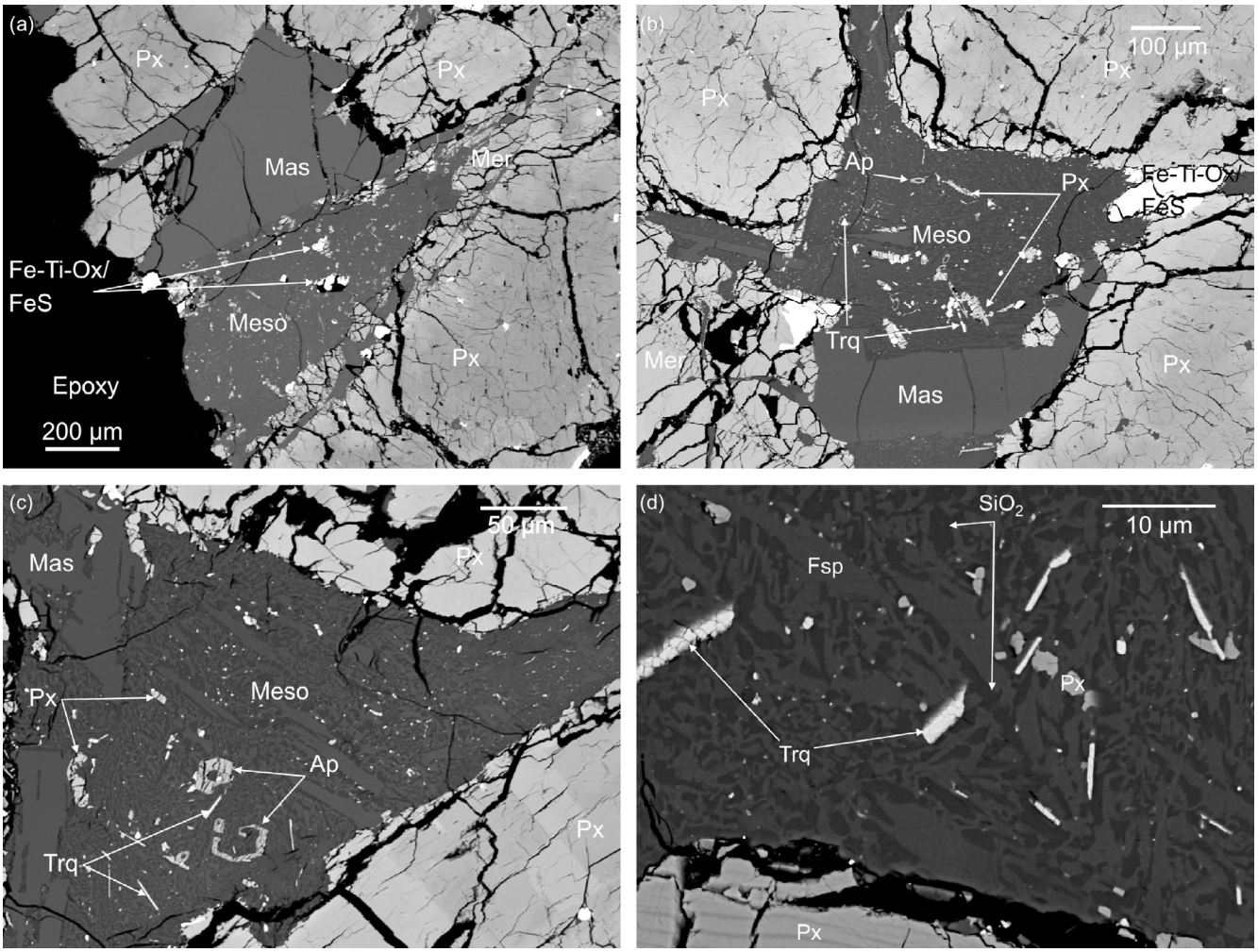

Fig. 4. BSE images of Si-rich mesostasis. a–c) Different sized Si-rich mesostasis areas. Cl-apatite within mesostasis typically shows skeletal growth. Other minor phases of mesostasis areas that are visible at these scales are tranquillityite, Fe-rich pyroxene, and Fe-Ti oxide or iron sulfide. d) Detailed image of tranquillityite grains within SiO_2 and feldspar intergrowth of a mesostasis area. Tranquillityite grains are heavily fractured. Px = pyroxene; Mas = maskelynite; Mer = merrillite; Ap = Cl-apatite; Meso =Si-rich mesostasis area; Fe-Ti-Ox/FeS = Fe-Ti oxide or iron sulfide; Trq = tranquillityite; SiO_2 = silica phase; Fsp = feldspar phase.

We studied tranquillityite using Raman spectrometry to contribute to its Raman characterization, as to our knowledge, only one tranquillityite Raman spectrum has so far been published (Chen et al., 2019). A representative Raman spectrum from grain tr_31_3 is shown in Fig. 3. The most prominent feature is a major, broad peak at 721.4 cm^{-1}. Smaller peaks are present at 120.7, 141.4, 179.6, 260, 309.6, 432.5, and 595.5 cm^{-1}. Additionally, two noticeable elevations in the intensity of the Raman signal are present in broader bands centered around 898 and 1218 cm^{-1}. The spectra from NWA 6963 tranquillityite are similar to the published spectra from Chen et al. (2019), with the differences that the center of the major peak is shifted by approximately 14 cm^{-1} to lower wave numbers and our measured spectra show a less prominent peak broadening of the major peak. However, peak broadening seems to still be present and suggests a reduced crystallinity of the grains (Chen et al., 2019). The cause for poor crystallinity might be the radioactive decay of U and Th that results in radiation damage of the crystal lattice (Gatehouse et al., 1977). Or the degraded crystallinity could be the result of shock. Further differences are the numerous weaker peaks at wave numbers <721.4 cm^{-1} which are not present in the literature spectrum. However, these peaks appear for all tranquillityite measurements at different locations and cannot be explained by surrounding phases of the Si-rich mesostasis; thus, these are interpreted to be part of the tranquillityite spectrum.

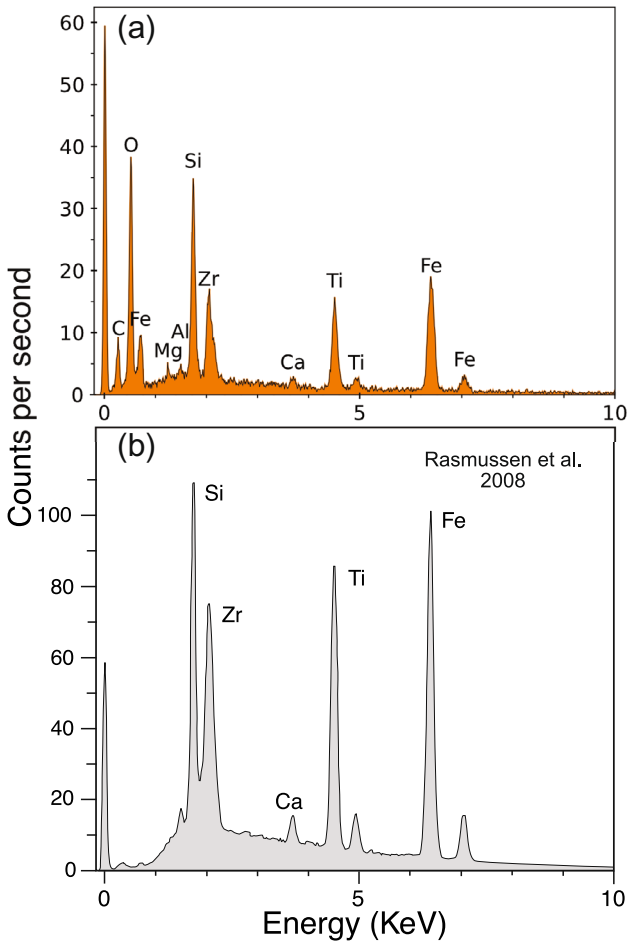

Fig. 5. SEM EDX spectra of tranquillityite. a) Representative EDX spectrum of tranquillityite, this study, lifetime was 10 s. The carbon peak is caused by a surficial carbon coating on the sample. b) Tranquillityite EDS spectrum from Rasmussen et al. (2008). (Color figure can be viewed at wileyonlinelibrary.com.)

Cl-apatite grains typically show skeletal growth and cores filled with material similar to the Si-rich mesostasis. Grain sizes range from approximately 2 μm × 2 μm to approximately 30 μm × 20 μm. SEM EDX measurements show a typical Cl-apatite spectrum with no F-peak present (Fig. S4 in supporting information). A representative Raman measurement on one Cl-apatite is shown in Fig. 3. The spectrum closely matches the Cl-apatite spectrum from the RRUFF database (Lafuente et al., 2016) taken as reference spectrum. Additionally, a measurement covering the range from 100 to 4000 cm^{-1} was made. No clear peak is visible in the region of 3500–3600 cm^{-1} in the background subtracted spectrum, where hydroxyl stretching vibrations should be measured, if a hydroxyapatite component were present (Cuscó et al., 1998; Ulian et al., 2013). However, the signal appears to be noisy and slightly elevated at just this position, and the presence of that component can thus neither be ruled out nor confirmed.

Only a few baddeleyite grains were found within the Si-rich mesostasis. Their grain sizes are below 5 μm × 5 μm and they are present as single grains or in small assemblages, in cases also including Fe-Ti oxide, pyroxene, and tranquillityite. One baddeleyite grain was measured with EPMA, but yielded totals lower than 98 wt%, likely because of the small grain size, or elements such as Hf not included in the measurements.

U–Pb Dating

U–Pb Dating of Merrillite

We performed 20 LA-MC-ICP-MS measurements on 11 individual merrillite grains dispersed along the thin section (Fig. S3 in supporting information). Using contrast-adjusted BSE images, we carefully studied each ablation spot for any presence of apatite and found none. EPMA measurements next to each ablation spot also always only confirmed merrillite. U–Pb results are listed in Table S5 in supporting information and plotted in a Tera–Wasserburg diagram (Fig. 6). The data form a well-defined linear array, with a regression that intersects the concordia at 178.3 ± 10.6 Ma (2σ, MSWD = 0.68, n = 20). This date is similar to crystallization ages published for enriched shergottites ranging from 225 to 165 Ma (Bellucci et al., 2018; Udry et al., 2020; Váci & Agee, 2020). The initial $^{207}Pb/^{206}Pb$-ratio derived from the y-intercept is 0.982 ± 0.007 (2σ), which as well falls in the range of published initial Pb isotopic compositions for enriched shergottites (Fig. 6) (Bellucci et al., 2015; Borg et al., 2005; Bouvier et al., 2005, 2008, 2009; McFarlane & Spray, 2022).

U–Pb Dating of Tranquillityite, Baddeleyite, Cl-Apatite, and Feldspar in the SiO_2-Rich Mesostasis

U–Pb results for minerals in the Si-rich mesostasis are shown in Fig. 6, plotted in a Tera–Wasserburg diagram, and listed in Table S6 in supporting information. Representative EDX spectra and image documentation of LA-MC-ICP-MS measurements can be found in Figs. S4 and S5 in supporting information, respectively. The $^{238}U/^{206}Pb$-ratios span a much wider range than for the merrillite, but define a similar, well-correlated linear array in Tera–Wasserburg space. The $^{238}U/^{206}Pb$ and $^{207}Pb/^{206}Pb$ ratios of the measurements vary, depending on the grain sizes of the ablated, U-containing minerals. For example, a negative correlation is seen between tranquillityite grain sizes versus $^{207}Pb/^{206}Pb$ ratios (Fig. S6 in supporting information).

Table 2. EPMA analyses (in wt%) on tranquillityite grains within Si-rich mesostasis in NWA 6963.

Tranquillityite									
SiO_2	16.31	16.03	20.32	17.5	20.17	16.19	15.64	18.79	16.41
TiO_2	20.02	20.20	18.29	18.84	18.52	20.18	20.6	19.33	21.54
Al_2O_3	0.70	0.66	1.29	1.03	1.59	0.86	0.70	1.42	0.81
Cr_2O_3	<0.11	<0.11	<0.11	<0.12	<0.12	<0.12	<0.12	<0.11	<0.11
MgO	1.47	1.07	1.54	1.52	1.46	1.58	1.54	1.51	1.64
FeO	45.79	45.82	44.29	45.11	45.86	46.58	46.53	45.59	45.44
MnO	0.54	0.56	0.45	0.56	0.59	0.52	0.58	0.64	0.49
NiO	<0.39	<0.38	<0.39	<0.39	<0.38	<0.40	<0.39	<0.39	<0.38
CaO	0.90	1.14	0.97	0.92	0.92	0.88	1.03	0.91	0.86
Na_2O	<0.02	<0.03	0.03	0.05	0.07	<0.02	<0.02	0.03	<0.02
K_2O	0.05	0.03	0.07	0.07	0.07	<0.02	0.05	0.07	0.10
P_2O_5	0.29	<0.26	0.30	<0.26	<0.25	<0.25	<0.25	0.29	0.46
ZrO_2	12.27	12.56	11.79	13.87	12.77	12.04	12.16	10.71	10.29
Y_3	<0.08	<0.08	<0.07	<0.08	<0.09	<0.07	<0.09	<0.07	<0.08
Rb	<0.02	0.02	0.04	<0.02	<0.02	<0.02	0.03	0.02	<0.02
Total[a]	98.34	98.09	99.38	99.47	102.02	98.83	98.86	99.31	98.04
Number of cations calculated on a basis of 24 O per formula unit									
Si	3.304	3.275	3.952	3.494	3.855	3.274	3.176	3.691	3.296
Ti	3.051	3.104	2.676	2.830	2.663	3.070	3.147	2.856	3.255
Al	0.167	0.159	0.296	0.242	0.358	0.205	0.168	0.329	0.192
Mg	0.444	0.326	0.447	0.452	0.416	0.476	0.466	0.442	0.491
Fe^{2+}	7.753	7.824	7.200	7.527	7.326	7.873	7.897	7.485	7.628
Mn	0.093	0.097	0.074	0.095	0.096	0.089	0.100	0.106	0.083
Ca	0.195	0.250	0.202	0.197	0.188	0.191	0.224	0.192	0.185
Na	b.d.	b.d.	0.011	0.019	0.026	b.d.	b.d.	0.011	b.d.
K	0.013	0.008	0.017	0.018	0.017	b.d.	0.013	0.018	0.026
P	0.050	b.d.	0.049	b.d.	b.d.	b.d.	b.d.	0.048	0.078
Zr	1.212	1.251	1.118	1.350	1.190	1.187	1.204	1.026	1.008
Rb	b.d.	0.003	0.005	b.d.	b.d.	b.d.	0.004	0.003	b.d.
$\Sigma_{Cations}$	16.281	16.296	16.048	16.224	16.135	16.366	16.398	16.206	16.241

b.d. = below detection limit.
[a]Totals are based on all elements as oxides.

This variation is likely due to the mixed analyses between tranquillityite with surrounding phases. This mixture, in combination with the applied constant correction for elemental fractionation for each spot (methods), may also cause a systematic error (see supplementary discussion). This error would systematically shift $^{238}U/^{206}Pb$ ratios to slightly higher values. The resulting value for the date derived from the intercept of the regression with the concordia line is thus a minimum value and the correct value could be up to 4.4 Ma higher (see supplementary discussion). The lowest $^{238}U/^{206}Pb$ and highest $^{207}Pb/^{206}Pb$ values are from two feldspar measurements, which anchor the data on the nonradiogenic side of the array. The regression through the data intersects the concordia at 172.4 ± 6.1 Ma (2σ, MSWD = 0.61, n = 30). This minimum date is indistinguishable within error from the date derived from the merrillite measurements. The initial $^{207}Pb/^{206}Pb$-ratio, as derived from the y-intercept of the regression, is 0.977 ± 0.003. The $^{207}Pb/^{206}Pb$-values from the mesostasis feldspar measurements are within error indistinguishable from the initial $^{207}Pb/^{206}Pb$-value derived from the merrillite data (Fig. 6; Tables S5 and S6).

DISCUSSION

Based on our results, we address the initial and main question of this study: Has the Si-rich mesostasis in enriched shergottites formed in (i) a late-stage crystallization product of relatively young, initially mafic melts as suggested by, for example, Stolper and McSween (1979) and Filiberto et al. (2014)? Or, (ii) by partial melting of the rock in response to an impact, as advocated by El Goresy et al. (2013)? Groundmass merrillite formed during late-stage crystallization of a magma (see below). If remaining silica-rich melt pockets formed in an igneous differentiation process co-

Table 3. Literature values (in wt%) of terrestrial (EPMA), lunar (EPMA), and Martian (TEM EDX) tranquillityite.

	Rasmussen et al. (2012)				Rasmussen et al. (2008)[a]	Meyer and Boctor (1974)[b]			Gancarz et al. (1972)[c]		El Goresy et al. (1972)	Lovering et al. (1971)[d]	Chen et al. (2019)	Li et al. (2021)[e]						Leroux and Cordier (2006)[f]
Body	Earth				Moon															Mars
SiO_2	15.22	15.63	17.02	18.61	14.97	13.90	14.70	13.30	15.43	14.55	15.20	14.00	15.10	16.44	14.28	13.73	13.07	14.64	17.65	16.75
TiO_2	23.63	22.74	22.76	24.46	20.43	21.20	20.50	20.70	21.19	23.90	23.00	19.45	19.80	15.42	15.97	16.90	16.80	16.71	15.07	19.92
Al_2O_3	0.67	0.60	0.55	1.72	1.13	1.02	1.22	0.89	0.88	1.24	1.76	1.12	1.11	1.48	1.48	1.44	1.45	1.50	1.41	0.91
Cr_2O_3	n.a.	n.a.	n.a.	n.a.	0.04	<0.01	<0.01	n.a.	0.01	0.07	n.a.	0.11	n.a.	0.02	0.01	0.01	0.03	0.00	0.01	n.a.
MgO	1.49	1.60	0.21	1.27	0.08	0.35	0.02	0.17	1.08	1.17	1.33	n.a.	0.04	0.04	0.04	0.04	0.02	0.03	0.06	1.49
FeO	45.59	45.53	43.82	43.74	42.71	42.40	40.90	41.10	43.20	42.28	41.40	42.48	45.30	44.87	44.38	45.52	45.79	44.64	44.78	45.85
MnO	0.44	0.42	0.54	0.45	0.34	0.09	0.35	0.04	0.34	0.27	n.a.	0.29	0.24	0.26	0.27	0.27	0.27	0.28	0.32	0.47
CaO	1.30	1.17	1.72	1.33	1.10	1.06	0.94	0.82	1.31	1.47	1.31	1.26	1.26	1.10	1.40	1.15	1.12	1.19	1.51	0.77
Na_2O	n.a.	n.a.	n.a.	n.a.	n.a.	n.a.	n.a.	n.a.	<0.01	0.02	n.a.	n.a.	n.a.	n.a.	n.a.	n.a.	n.a.	n.a.	n.a.	n.a.
K_2O	n.a.	n.a.	n.a.	n.a.	n.a.	n.a.	n.a.	n.a.	<0.01	0.02	n.a.	n.a.	n.a.	n.a.	n.a.	n.a.	n.a.	n.a.	n.a.	n.a.
P_2O_5	n.a.	n.a.	n.a.	n.a.	n.a.	<0.01	<0.01	n.a.	0.03	0.26	n.a.	n.a.	n.a.	n.a.	n.a.	n.a.	n.a.	n.a.	n.a.	n.a.
ZrO_2	9.93	10.98	9.00	6.96	14.17	16.20	18.50	17.00	13.21	11.27	12.60	17.15	14.6	16.80	18.18	18.08	17.87	17.73	16.49	13.83
Y_2O	0.17	0.21	1.20	1.00	2.50	3.01	2.69	3.56	0.27	0.60	1.60	2.76	0.45	0.60	0.68	0.61	0.59	0.59	0.57	n.a.
Nb_2O_5	0.26	0.18	0.19	0.32	0.74	0.68	0.82	0.59	<0.01	<0.01	n.a.	0.33	n.a.	0.38	0.45	0.36	0.36	0.35	0.56	n.a.
REE_2O_3	0.43	0.38	0.83	0.95	1.89	0.02	0.30	0.90	0.48	0.40	n.a.	0.24	0.08	0.73	0.75	0.63	0.58	0.60	0.55	n.a.
HfO_2	0.11	0.11	0.12	0.10	0.29	0.25	0.25	0.17	0.72	0.55	0.45	0.17	0.47	0.41	0.46	0.39	0.40	0.44	0.42	n.a.
Total	99.24	99.55	97.96	100.91	100.5	100.21	101.22	99.15	98.30	98.39	98.65	99.36	98.45	98.57	98.34	99.12	98.35	98.71	99.41	100.00
Number of cations calculated on a basis of 24 O per formula unit																				
Si	3.052	3.128	3.434	3.550	3.049	2.832	2.956	2.731	3.149	2.936	3.042	2.896	3.115	3.413	3.019	2.889	2.786	3.065	3.603	3.341
Ti	3.565	3.423	3.455	3.510	3.131	3.249	3.101	3.247	3.253	3.628	3.463	3.027	3.073	2.409	2.540	2.675	2.695	2.631	2.314	2.989
Al	0.158	0.142	0.131	0.387	0.271	0.245	0.289	0.219	0.212	0.295	0.415	0.273	0.270	0.361	0.369	0.357	0.364	0.369	0.339	0.214
Cr	n.a.	n.a.	n.a.	n.a.	0.006	n.a.	n.a.	n.a.	0.002	0.011	n.a.	0.018	n.a.	0.004	0.001	0.002	0.004	0.000	0.001	n.a.
Mg	0.445	0.477	0.063	0.361	0.024	0.106	0.006	0.053	0.329	0.352	0.397	n.a.	0.012	0.013	0.012	0.011	0.007	0.008	0.017	0.444
Fe^{2+}	7.642	7.616	7.391	6.974	7.272	7.220	6.874	7.163	7.368	7.131	6.925	7.346	7.811	7.787	7.843	8.005	8.161	7.812	7.640	7.642
Mn	0.075	0.071	0.092	0.073	0.059	0.016	0.060	0.007	0.059	0.046	n.a.	0.051	0.042	0.046	0.049	0.048	0.048	0.050	0.056	0.080
Ca	0.279	0.251	0.372	0.272	0.240	0.231	0.203	0.183	0.286	0.318	0.281	0.279	0.278	0.246	0.316	0.259	0.257	0.267	0.330	0.164
Na	n.a.	n.a.	n.a.	n.a.	n.a.	n.a.	n.a.	n.a.	n.a.	0.008	n.a.	n.a.	n.a.	n.a.	n.a.	n.a.	n.a.	n.a.	n.a.	n.a.
K	n.a.	n.a.	n.a.	n.a.	n.a.	n.a.	n.a.	n.a.	n.a.	0.005	n.a.	n.a.	n.a.	n.a.	n.a.	n.a.	n.a.	n.a.	n.a.	n.a.
P	n.a.	n.a.	n.a.	n.a.	n.a.	n.a.	n.a.	n.a.	0.005	0.044	n.a.	n.a.	n.a.	n.a.	n.a.	n.a.	n.a.	n.a.	n.a.	n.a.
Zr	0.971	1.071	0.886	0.647	1.407	1.609	1.814	1.728	1.314	1.109	1.230	1.730	1.469	1.701	1.875	1.855	1.858	1.810	1.642	1.344
Y	0.018	0.022	0.129	0.102	0.271	0.326	0.288	0.395	0.029	0.064	0.170	0.304	0.049	0.066	0.076	0.069	0.067	0.066	0.062	n.a.
Nb	0.024	0.016	0.017	0.028	0.068	0.063	0.075	0.056	n.a.	n.a.	n.a.	0.031	n.a.	0.036	0.043	0.034	0.035	0.033	0.051	n.a.
REE total	0.031	0.027	0.057	0.062	0.127	0.001	0.022	0.060	0.035	0.029	n.a.	0.018	0.006	0.051	0.053	0.043	0.040	0.041	0.036	n.a.
Hf	0.006	0.006	0.007	0.005	0.017	0.015	0.014	0.010	0.042	0.032	0.026	0.010	0.028	0.024	0.028	0.024	0.025	0.026	0.024	n.a.
$\Sigma_{Cations}$	16.267	16.251	16.034	15.971	15.949	15.914	15.702	15.858	16.090	16.023	15.948	15.983	16.153	16.157	16.224	16.271	16.347	16.179	16.118	16.219

Oxide wt% values are taken from references, apfu values are then calculated from oxide values for all literature compositions after Deer et al. (2013).
n.a. = not analyzed/not given.
[a]Rasmussen et al. (2008) additionally report Ta_2O_5: 0.04 wt%, WO_3: 0.03 wt%, and PbO: 0.04 wt%.
[b]Meyer and Boctor (1974) additionally report for 1&2: Ta_2O_5: <0.01 wt%, Th_2O: 0.03 wt%, and for 3: Ta_2O_5: <0.01 wt%, Th_2O: 0.11 wt%.
[c]Gancarz et al. (1972) additionally report for 1: PbO: 0.04 wt%, Th_2O: 0.03 wt%, UO_2: 0.08 wt%, and for 2: PbO: 0.03 wt%, Th_2O: 0.08 wt%, UO_2: 0.21 wt%.
[d]The average of 12 measurements as published by Lovering et al. (1971).
[e]Li et al. (2021) additionally report 0.01 wt%, 0.02 wt%, and 0.03 wt% Ta_2O_5 for 1, 5, and 6, respectively.
[f]This is a TEM EDX measurement, reported by Leroux and Cordier (2006) in at% and here calculated to oxide wt%.

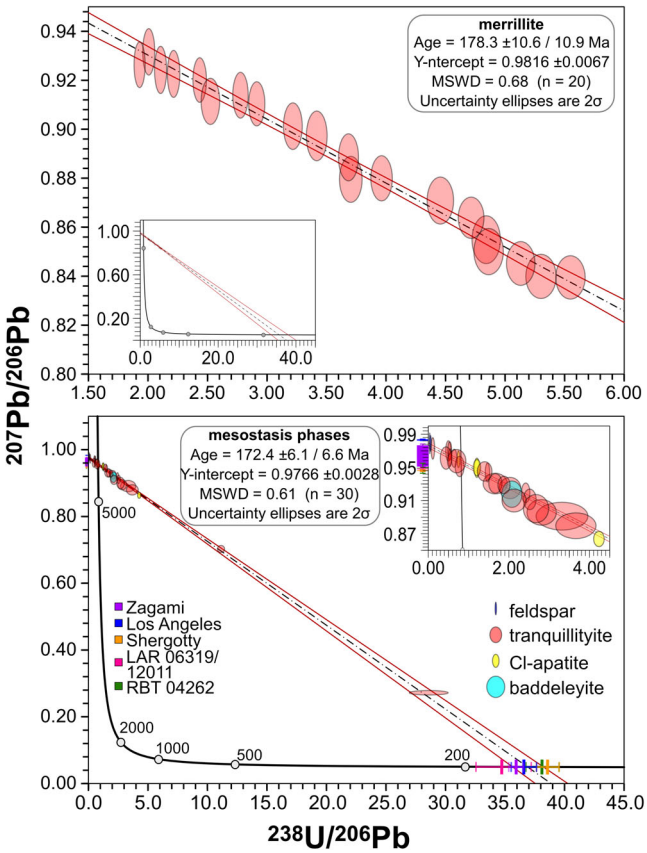

Fig. 6. Tera–Wasserburg plots of the U–Pb data for coarse-grained merrillite and for tranquillityite, apatite, baddeleyite, and feldspar in the Si-rich mesostasis. Axes units are $^{207}Pb/^{206}Pb$ and $^{238}U/^{206}Pb$ ratios, not corrected for initial Pb, as given in Tables S5 and S6. Upper: Merrillite data. The dashed line is the regression line through the data points. Red lines are 2σ uncertainty envelopes for the regression line; the inset shows the full regression line, which intersects the concordia (black curve) at 178.3 ± 10.6 Ma. Lower: Mesostasis mineral U–Pb data collected from the measurements of tranquillityite, apatite, baddeleyite, and feldspar are shown together with a full regression line through the data points. The regression line intersects the concordia (black curve, open points mark different intercept ages in Ma) at 172.4 ± 6.1 Ma. Shown for comparison are literature values of enriched shergottites of their initial $^{207}Pb/^{206}Pb$ plotted at the *y*-axis, and of their crystallization age plotted onto the concordia line. The inset shows an enlarged view of the region with the highest density of data points. Regression line envelopes are 2σ uncertainties. Data: initial $^{207}Pb/^{206}Pb$: Zagami: Bellucci et al. (2015), Borg et al. (2005), Bouvier et al. (2005); Los Angeles: McFarlane and Spray (2022), Bouvier et al. (2005), Shergotty: Bouvier et al. (2008), Larkman Nunatak [LAR] 12011: Bellucci et al. (2015), Roberts Massif [RBT] 04262: Bouvier et al. (2009), Bellucci et al. (2015); crystallization age: Zagami, Shergotty: Nyquist et al. (2001), Los Angeles: McFarlane and Spray (2022), RBT 04262: Shih et al. (2009), LAR 06319: Shafer et al. (2010). (Color figure can be viewed at wileyonlinelibrary.com.)

genetically with the merrillite, their age should be similar, and such melt pockets would now represent the Si-rich mesostasis. In contrast, the age of the Si-rich mesostasis would most certainly be younger than the groundmass merrillite, should the Si-rich mesostasis have formed later during a shock event. We first discuss the age and formation scenarios of merrillite and the Si-rich mesostasis, before we conclude on the implications of these ages regarding the formation of the Si-rich mesostasis.

Formation and Age of Merrillite

Formation

Merrillite is interpreted to be a late-stage crystallizing phase in Martian meteorites (Shearer et al., 2015). Nonetheless, merrillite was observed as a liquidus phase in shergottite melt crystallization experiments (Herd et al., 2004). Wenzel et al. (2021) constrained the crystallization sequence of NWA 6963 using pyroxene zoning profiles, and concluded that minor phases such as Fe-Ti oxide or sulfide and phosphates crystallized after simultaneous growth of Fe-rich pigeonite rims around cumulus pyroxene cores and crystallization of plagioclase. This sequence is in accordance with the frequent observation that merrillite, Fe-Ti oxide, and Fe-sulfide grains are spatially associated with Si-rich mesostasis areas in NWA 6963, suggesting the crystallization of later phases in interstices produced by pyroxene rim growth and plagioclase crystallization. Jolliff et al. (1993) found substantially higher Mg# in lunar merrillites than in coexisting pigeonite and higher than in coexisting augite. They observed this trend for merrillites with a range in Mg# from 40 to 95. The relatively low Mg-merrillite component (Mg# from 45 to 56, Table 1) observed here thus also indicates that the grains did not crystallize simultaneously with pyroxene cores that were measured in the study of Wenzel et al. (2021). These all have Mg# equal to or higher than 50, except for their Pyroxene 3, where the zoning profile does not intersect the highest Mg regions of the core. Based on these observations, and together with the coarse-grained size of merrillite and their textural relationship to other coarse-grained groundmass minerals, we conclude that merrillite crystals formed magmatically at a later stage in the crystallization sequence.

Hughes et al. (2008) showed that merrillite and H-bearing whitlockite form a solid solution at hydrothermal conditions (550 °C). Shearer et al. (2015) used this to suggest that hydrothermal alteration of merrillite to whitlockite might produce an additional Raman peak because of HPO_4^{2-} in the whitlockite. More recently, however, Adcock et al. (2017) showed that dehydrogenation from whitlockite to merrillite can occur due to high temperatures (>1000 °C) potentially reached during impact-induced shock. Hence, a shock

event could have erased any sign of whitlockite, and merrillite in shergottites could originally indeed have been whitlockite that formed either directly from the magma or from hydrous alteration of magmatic merrillite. Selin et al. (2014) assumed that groundmass apatite in NWA 6963 crystallized from the melt; however, Słaby et al. (2017) suggested a late metasomatic event to explain apatite, in particular in Cl-apatite regions associated with merrillite grains in enriched shergottite NWA 2975. It cannot be excluded that such an event could have altered magmatic merrillite into Cl-apatite also in NWA 6963.

In summary, while we show that merrillite crystals in NWA 6963 formed magmatically, metasomatism of merrillite might have formed associated Cl-apatite regions within merrillite (Słaby et al., 2017). We observe no tell-tale whitlockite peak in our merrillite spectra, thus, should further hydrothermal alteration have affected merrillite grains in NWA 6963, this was limited to the formation of Cl-apatite and no extensive, fluid-induced hydrothermal alteration affected most of the merrillite (Shearer et al., 2015) or shock-induced dehydrogenation from whitlockite to merrillite removed any other signs of hydrous alteration of merrillite (Adcock et al., 2017). We did not observe shock-induced transformation from merrillite into its high-pressure form tuite (Wang et al., 2017; Xie et al., 2002, 2004, 2013; Yoshida et al., 2021). Tuite (with an ideal formula of $Ca_3[PO_4]_2$) has previously been found in enriched shergottites (Boonsue & Spray, 2012; Wang et al., 2017; Yoshida et al., 2021); however, the occurrence was restricted to smaller grains (≤100 μm) located within shock melt veins only, where a high temperature during the shock event is expected (Wang et al., 2017). Tuite, if generated by shock from merrillite, is chemically indistinguishable from its precursor phase (Xie et al., 2013, 2016), but recognizable due to a different Raman spectrum. One merrillite grain (GGMer4; Fig. 2c and 2d) is in contact to a small (35 μm in width) shock melt vein and yields a Raman spectrum of merrillite. This spectrum is measured next to a U–Pb dating spot, at a distance of 350 μm to the contact to the shock melt vein. Notably, both U–Pb dating spots (at distances of 350 and 160 μm to the contact, respectively) show no deviation from the regression through the merrillite U–Pb data points, indicative of no modification of U and Pb. Thus, while phase transformation from merrillite to tuite might occur within shock melt veins as observed in other enriched shergottites (Boonsue & Spray, 2012; Wang et al., 2017; Yoshida et al., 2021), this transformation does not affect whole grains at observed grain sizes for merrillite in NWA 6963, even if these are in contact with small shock melt veins.

Age

The date of 178.3 ± 10.6 Ma and initial $^{207}Pb/^{206}Pb$-value derived by merrillite U–Pb measurements (Fig. 6) is in agreement with previously published ages and Pb initials of enriched shergottites (Bellucci et al., 2015, 2018; Borg et al., 2005; Bouvier et al., 2005, 2008, 2009; McFarlane & Spray, 2022; Udry et al., 2020; Váci & Agee, 2020). This indicates that the date can be interpreted as a robust age for the crystallization of NWA 6963 groundmass merrillites. A common crystallization age and only very low modification of the U–Pb isotopic system are further supported by the low scatter of our data around the regression line (Ludwig, 1998). Apparently, the merrillite crystals experienced only minor, if at all Pb- or U-loss or addition since their formation, and neither the shock nor any metasomatism disturbed the U–Pb system. These only small—if any—changes of Pb- or U-concentrations are additional evidence for an absence of hydrothermal alteration of merrillite to whitlockite. We thus interpret the derived date as a crystallization age for groundmass merrillite within NWA 6963.

Age and Formation of the Si-Rich Mesostasis

Tranquillityite

Tranquillityite constitutes the majority of grains we used for U–Pb dating of Si-rich mesostasis. The mineral might undergo various alterations: Rasmussen et al. (2008) observed isochemical decomposition of lunar tranquillityite into zirconolite, fayalite, ilmenite, and baddeleyite. El Goresy et al. (1974) described a similar tranquillityite decomposition into baddeleyite, ilmenite, and pyroxene. Rasmussen et al. (2012) observed an alteration of tranquillityite to smaller secondary phases in terrestrial samples. In particular, such alteration is described by Rasmussen et al. (2008, 2012) as patches of replacive mineral intergrowths within the tranquillityite grains. The replacive, secondary phases are much smaller in grain size than the original tranquillityite crystals. This kind of alteration was not observed in the tranquillityite studied here. Instead, these grains are intensively fractured, presumably as an effect of shock. However, small individual assemblages of pyroxene, Fe-Ti oxide, and baddeleyite are observed within the Si-rich mesostasis, which might in combination with SiO_2 represent decomposed tranquillityite. In contrast to the above-described alteration, however, the grain sizes of these phases are in the range of the tranquillityite grains found within the Si-rich mesostasis. They indicate the formation of these phases instead of tranquillityite, rather than from tranquillityite. This could point to localized varying abundances of tranquillityite-stabilizing elements like Zr

and Y during the last stages of crystallization of mesostasis domains. The low Zr and Y abundances in NWA 6963 (and NWA 856) tranquillityites of 10.3–13.9 wt% (and Y concentrations below detection limit) might then represent a value close to the minimum concentrations required for stabilizing this phase during the cooling history of the rock.

Cl-Apatite and Baddeleyite

U–Pb measurements of Cl-apatite and baddeleyite plot close to the majority of the tranquillityite data in the Tera–Wasserburg plot. Cl-apatite and baddeleyite grains are small, and the data are mixtures with the surrounding mesostasis phases. Both Cl-apatite and baddeleyite contain considerable amounts of U and measurements of Cl-apatite cover a range of $^{207}Pb/^{206}Pb$ versus $^{238}U/^{206}Pb$ similar to merrillite (Fig. 6). However, it is possible that mixtures with adjacent tranquillityite also contribute to higher $^{238}U/^{206}Pb$ ratios. The accordance with tranquillityite and feldspar U–Pb data on one regression indicates that Cl-apatite and baddeleyite were also robust against U and Pb modification.

Feldspar

Mesostasis feldspar measurements have very low $^{238}U/^{206}Pb$ and serve as anchor on the nonradiogenic side of the array, thereby increasing the precision of the derived date. It is suggested that the feldspar is amorphous (Hamilton & Filiberto, 2015) as a result of shock. However, apparently no significant U or radiogenic Pb incorporation happened during amorphization and shock, despite the presence of U-rich phases like tranquillityite within the feldspar–silica intergrowth. Conversely, this indicates that the mesostasis feldspar indeed originally crystallized as mineral and was not quenched to an amorphous feldspatic phase during cooling of the rock, as the U-exclusion is a characteristic of the feldspar crystal structure (Zartman & Wasserburg, 1969).

Age

The U–Pb intercept date of 172.4 ± 6.1 Ma derived from Si-rich mesostasis minerals tranquillityite, Cl-apatite, baddeleyite, and feldspar (Fig. 6) has a higher precision than the merrillite date, because of higher $^{238}U/^{206}Pb$ and lower $^{207}Pb/^{206}Pb$ ratios in two measured tranquillityite grains, and feldspar values indistinguishable from derived initial $^{207}Pb/^{206}Pb$. As described above, tranquillityite seems unaltered. Furthermore, the mesostasis mineral U–Pb data derived from measurements dispersed throughout the sample form a well-defined array with low scatter around the regression line, indicative of no U- or Pb-loss or addition, and a common crystallization age for all sampled phases (Ludwig, 1998). Processes causing U- or Pb-loss or addition should affect each grain individually, leading to large scatters of the data, rather than the observed well-defined array. Because of the measurement spots being mixtures with surrounding phases, which might lead to slightly too high $^{238}U/^{206}Pb$ ratios (see methods, supplementary discussion), we interpret the date of 172.4 ± 6.1 Ma of the Si-rich mesostasis grains in NWA 6963 (Fig. 6) as the minimum crystallization age of these minerals and hence, also of the Si-rich mesostasis itself.

The Origin of the Si-Rich Mesostasis

The date interpreted as the minimum crystallization age for the Si-rich mesostasis is, within error, indistinguishable from the date interpreted as the crystallization age for the groundmass merrillites—and in agreement with the published crystallization ages for other enriched shergottites (Udry et al., 2020; Váci & Agee, 2020). Note that analytical admixing of feldspar and/or other mesostasis phases during laser ablation analyses of mesostasis minerals may have produced a small systematic error, such that the true age may be up to 4.4 Ma older (see supplementary discussion). An impact event could have provided the required energy to partially melt the source rock, producing the Si-rich mesostasis. Such an event should not have melted the entire rock, as its texture disagrees with an expected fast cooling after a shock event. Additionally, the texture of the Si-rich mesostasis disagrees with the texture observed for shock melts within enriched shergottite Los Angeles (Walton & Spray, 2003) and within other intermediate shergottites (Walton et al., 2012; Walton & Herd, 2007). Furthermore, such an event would have needed to occur comparatively shortly after the emplacement of the source rock (178.3 ± 10.6 Ma, the age of magmatically formed merrillite), that is, within the error of the determined age, which is ±10.6 million years. Although not impossible, we regard this an unlikely coincidence, and therefore exclude the formation of the Si-rich mesostasis by shock.

We note, however, that Adcock et al. (2017) argued for the complete transformation of whitlockite to merrillite in shergottites during a shock event. Such a shock event could have reset the U–Pb system in the resulting merrillite. If the Si-rich mesostasis formed in the same shock event that would have also formed merrillite by dehydrogenation of precursor whitlockite (Adcock et al., 2017), the same age of the merrillite and Si-rich mesostasis would be expected and represents the shock event at a time of approximately 174 Ma (weighted average of our derived ages, see below), which is what we observe. However, to maintain charge

balance during the transformation from whitlockite to merrillite, Adcock et al. (2017) suggested that additional minor Ca-phosphate minerals, with a low Ca:P ratios, form. The authors stated that such minor phases in shergottite merrillite might provide evidence for a transformation during shock. We did not notice such phases during investigation of merrillite with SEM. Additionally, we used EMPA chemical mapping (WDS and EDS) of five merrillite grains to specifically search for these phases but were not able to find any (Fig. S7 in supporting information). We thus conclude that the merrillite did not form by transformation from whitlockite (due to shock or otherwise). In addition, enriched shergottites have CRE ages between 1 and 6 Ma (Herzog & Caffee, 2014; Wieler et al., 2016). To our knowledge, no cosmic ray exposure (CRE) age has been reported for NWA 6963. However, as NWA 6963 has the same geochemical characteristics as other enriched shergottites, as well as similar crystallization ages (Bellucci et al., 2018; Udry et al., 2020; Váci & Agee, 2020), while speculative, it appears unlikely that NWA 6963 has a largely different CRE age (i.e., $\gg$6 Ma) than other enriched shergottites. If Si-rich mesostases formed approximately 174 Ma ago from an impact shock, and NWA 6963 itself was sent on its way to the Earth after an impact shock 1–6 Ma ago—the exact same spot on Mars must have been hit twice by a large asteroid—and further in the first impact approximately 174 Ma ago, the U–Pb system in merrillite was reset, whitlockite transformed to merrillite, Si-rich mesostases was produced, and the rock remained on Mars. Conversely, in the second impact, the U–Pb system remained undisturbed; no Si-rich mesostases formed or was reset; and the rock was now ejected from Mars and sent on its way to the Earth. While this might be considered a possible scenario, it seems a highly unlikely chain of events. A final argument against the impact origin of the Si-rich mesostasis is derived from its chemical composition, which is near-eutectic, and enriched in incompatible elements, as it is expected from a differentiated, late-stage melt. An impact melt, in contrast, would likely be highly heterogenous depending on the modes of the instantaneously molten minerals, as has been shown for Los Angeles (Walton & Spray, 2003). There is no reason why locally fused domains of the rock should be consistently enriched in incompatible elements like Zr.

We note that there is a strong contrast in grain size between the fine-grained late-stage Si-rich mesostasis (1–35 μm), the coarse-grained pyroxene and plagioclase, and the coarse-grained merrillite (0.1–1 mm). The latter is also interpreted as a late-stage magmatic phase. That contrast indicates a sudden change to higher crystallization rates during the time of Si-rich mesostasis crystallization. Following Filiberto et al. (2018), this change might have been induced at the time of transport of the magma from a deep-seated crustal chamber, where the pyroxene cores and some plagioclase formed, to the Martian shallow subsurface, where finally the remaining, interstitial, near-eutectic melt rapidly crystallized in the form of a graphic intergrowth of a silica polymorph and alkali feldspar (Filiberto et al., 2018; Wenzel et al., 2021). Further studies are needed to fully understand the crystallization history of the rock.

Our results—based on rock ages—therefore favor the formation of Si-rich mesostasis in the late stage of source rock crystallization. In view of the geochemical similarities of enriched shergottites (e.g., Udry et al., 2020) and the widespread occurrence of Si-rich mesostasis in these samples (e.g., Leroux & Cordier, 2006; Sheen et al., 2021), our results thus support the conclusion of a late-stage crystallization of Si-rich mesostasis in enriched shergottites as presented by, for example, Stolper and McSween (1979), Leroux and Cordier (2006), Filiberto et al. (2014), and Wu et al. (2021).

Shock

The absence of tuite in the groundmass allows us to conclude on qualitative constraints of effective shock-induced *P*–*T* conditions experienced by the merrillite grains. Filiberto et al. (2018) estimated shock pressures for NWA 6963 between 38 and 45 GPa. The post-shock temperature increase was estimated to be 100–600 °C (Filiberto et al., 2018). The merrillite–tuite phase transition is expected to occur at *P*–*T* conditions above 12 GPa at 2300 °C to 15 GPa at 1100 °C (Xie et al., 2013). The absence of tuite, despite estimated shock pressures for groundmass minerals that are well above the merrillite–tuite transition, has also been observed for Los Angeles (Britvin et al., 2016). However, this is not necessarily in disagreement. The post-shock temperature increase might have been too low to raise the temperature above the inferred temperature of 1100 °C for the merrillite–tuite transformation (Xie et al., 2013). It is possible that merrillite is stable over a wider pressure range at lower temperatures, as the system is not well known under these conditions, and only roughly constrained after the apatite–tuite transition (Murayama et al., 1986; Thompson et al., 2013; Xie et al., 2016). However, the apatite–tuite phase boundary has a negative Clapeyron slope and it is suggested that the apatite–tuite (and thus possibly the merrillite–tuite) phase transition also occurs at lower temperatures at pressure conditions that are still below the inferred minimum shock pressure of

38 GPa for NWA 6963 (Filiberto et al., 2018; Murayama et al., 1986). Thus, another possibility is that the temperature was increased above the temperature of the merrillite–tuite transition, but the transformation might be a kinetically controlled process that required either longer durations of the high-pressure conditions during the post-shock temperature increase or higher temperatures to facilitate the phase transformation (Fritz et al., 2017). A kinetically controlled phase transformation would also be in accordance with the shock experiments of Adcock et al. (2017), that were conducted above the pressures for the inferred merrillite–tuite transition, and as the authors show, likely above the temperatures, but where no tuite was reported (Adcock et al., 2017). It can be concluded that the transient conditions of the shock-induced *P*–*T* path experienced by the target rock were probably too low for a transformation of groundmass merrillite grains to tuite during the short duration of high-pressure conditions. Instead, they led to intensive fracturing of the merrillite grains (cf. Britvin et al., 2016). Importantly, this had no significant effect on the U–Pb system of measured merrillite grains, as U–Pb modifications would introduce scatter around the regression line (i.e., would likely shift data points to the right, in cases where grains suffered Pb-loss; cf. McFarlane & Spray, 2022). However, the conditions to form tuite might possibly be reached locally, at temperature hotspots, that are now represented by shock melt veins or pockets, as observed for other enriched shergottites (Boonsue & Spray, 2012; Wang et al., 2017; Yoshida et al., 2021). Within or in very close contact to these hotspot locations (irrespective of tuite formation from merrillite), a modification of the U–Pb system of merrillite grains would be more likely to occur (McFarlane & Spray, 2022). Note, however, that we observe no modification at greater distance to such contacts (≥160 μm in distance from a contact to a small 35 μm shock melt vein at U–Pb spot 2 within grain GGMer4 in Fig. S3 and Fig. 2, see also above), which further attests to the robustness of merrillite grains against U–Pb disturbance.

Shock effects, like the formation of maskelynite, deformation features within pyroxene (Filiberto et al., 2018), and extensive fracturing of merrillite grains, are observed throughout the sample. It is, thus, likely that shock also affected the Si-rich mesostasis. Textural evidence for that comes in the form of the extensive fracturing of tranquillityite grains within Si-rich mesostasis (Fig. 4d), and the silica and feldspar grains of the Si-rich mesostasis being amorphous rather than crystalline, which has been attributed to shock (Hamilton & Filiberto, 2015). Our data allow limited constraints on the experienced temperature conditions: The Raman measurement of one Cl-apatite grain gives a clear Cl-apatite spectrum (Fig. 3b). This indicates that Cl-apatite within Si-rich mesostasis, despite the small grain sizes, did not transform into tuite, which leads to a similar conclusion as for the absence of tuite formed from merrillite (see above). An upper temperature limit might be given by the breakdown temperature of tranquillityite at 900 °C (Gatehouse et al., 1977). Using SEM, we observe tranquillityite grains smaller than 1 μm in width (Fig. 4d), likely susceptible to break down if this temperature would have been reached. Consequently, we regard it unlikely that the post-shock temperature increase led to temperatures above 900 °C within the Si-rich mesostasis, and probably within the whole sample, except for distinct temperature hotspots, now represented by shock melt veins.

Implications

Si-rich mesostasis in NWA 6963 and likely in other enriched shergottites is a product of magmatic differentiation and not of shock. This conclusion is in agreement with conclusions of previous studies (Filiberto et al., 2014; Herd et al., 2018; Leroux & Cordier, 2006; Stolper & McSween, 1979; Wu et al., 2021). Next to magmatic inclusions (Ikeda, 2005) and evolved igneous clasts within the regolith breccia NWA 7034 and paired stones (Humayun et al., 2013; Lindner et al., 2020), these areas are rare samples of highly differentiated melts form Mars, which are accessible in laboratories on Earth. They allow a more complete investigation of the differentiation pathways of the young (225–165 Ma; Udry et al., 2020; Váci & Agee, 2020) enriched shergottite melts. Although the observed volumes of Si-rich melt within enriched shergottites are small, and thus, comparability is questionable, improvement on the knowledge about processes leading to evolved rocks on Mars is generally important, as more felsic lithologies were recently discovered on Mars by remote-sensing orbiters and rovers (Carter & Poulet, 2013; Sautter et al., 2015; Wray et al., 2013) or are suggested to be present within the Martian curst by recent density estimations (Knapmeyer-Endrun et al., 2021).

CONCLUSIONS

The groundmass merrillite as well as the Si-rich mesostasis in NWA 6963 have the same age within error of 178.3 ± 10.6 Ma and 172.4 ± 6.1 Ma, respectively. These indistinguishable ages are best explained by a co-genetic formation of the Si-rich mesostasis with its host rock, that is, as a late-stage

crystallization product after magma emplacement. The crystallization age of NWA 6963 might therefore be given as 174 ± 6 Ma, which is the weighted mean of the two derived ages. Our results are in favor of a magmatic origin of Si-rich mesostasis in enriched shergottites, as opposed to shock-induced formation. It has been shown before that lunar and terrestrial tranquillityite can be used to derive Pb–Pb crystallization ages by in situ ion probe techniques (Andersen & Hinthorne, 1972; Rasmussen et al., 2008, 2012; Tartèse et al., 2013). Tranquillityite has recently been used for Pb–Pb dating of returned lunar samples (Li et al., 2021). Here, we have shown that tranquillityite is also useful for in situ U–Pb dating by LA-(MC-)ICP-MS and extend its applicability to Martian meteorites.

We finally note, based on the abundance of phosphates in rocks from Gusev crater (McSween, 2015), that these are promising candidates for U–Pb chronology for the scheduled sample return mission of rocks from Jezero Crater.

Acknowledgments—We would like to thank Linda Marko and Dr. Alexander Schmidt for the help with the U–Pb measurements, Lea Ruckes for the help with EPMA measurements, and Philomena Genzel for the help with Raman measurements. We would like to thank Vivien Sauer for prior SEM work on the sample that provided part of the BSE images used during this study. We are grateful for thorough reviews and constructive feedback by Geoffrey Howarth, Arya Udry, and Joshua Snape, which vastly improved the paper. We would like to thank Katherine Joy for further constructive feedback and comments and editorial handling. Finally, we like to thank the Dr. Rolf M. Schwiete-Stiftung for financial support. FIERCE is financially supported by the Wilhelm and Else Heraeus Foundation and by the Deutsche Forschungsgemeinschaft (DFG, INST 161/921-1 FUGG and INST 161/923-1 FUGG) which is gratefully acknowledged. This is FIERCE contribution No. 111. Open Access funding enabled and organized by Projekt DEAL.

Conflict of Interest—The authors declare no conflicts of interest.

Data Availability Statement—The data that support the findings of this study are available in the article and the supplementary material of this article.

Editorial Handling—Dr. Katherine Helen Joy

REFERENCES

Adcock, C. T., Tschauner, O., Hausrath, E. M., Udry, A., Luo, S. N., Cai, Y., Ren, M., et al. 2017. Shock-Transformation of Whitlockite to Merrillite and the Implications for Meteoritic Phosphate. *Nature Communications* 8: 14667. https://doi.org/10.1038/ncomms14667.

Andersen, C. A., and Hinthorne, J. R. 1972. U, Th, Pb, and REE Abundances and $^{207}Pb/^{206}Pb$ Ages of Individual Minerals in Returned Lunar Material by Ion Microprobe Mass Analysis. *Earth and Planetary Science Letters* 14: 195–200.

Banerdt, W. B., Smrekar, S. E., Banfield, D., Giardini, D., Golombek, M., Johnson, C. L., Lognonné, P., et al. 2020. Initial Results from the InSight Mission on Mars. *Nature Geoscience* 13: 183–9. https://doi.org/10.1038/s41561-020-0544-y.

Bellucci, J. J., Nemchin, A. A., Whitehouse, M. J., Snape, J. F., Bland, P., and Benedix, G. K. 2015. The Pb Isotopic Evolution of the Martian Mantle Constrained by Initial Pb in Martian Meteorites. *Journal of Geophysical Research: Planets* 120: 2224–40. https://doi.org/10.1002/2015JE004809.

Bellucci, J. J., Nemchin, A. A., Whitehouse, M. J., Snape, J. F., Bland, P., Benedix, G. K., and Roszjar, J. 2018. Pb Evolution in the Martian Mantle. *Earth and Planetary Science Letters* 485: 79–87. https://doi.org/10.1016/j.epsl.2017.12.039.

Boonsue, S., and Spray, J. 2012. Shock-Induced Phase Transformations in Melt Pockets Within Martian Meteorite NWA 4468. *Spectroscopy Letters* 45: 127–34. https://doi.org/10.1080/00387010.2011.614670.

Borg, L. E., Edmunson, J. E., and Asmerom, Y. 2005. Constraints on the U-Pb Isotopic Systematics of Mars Inferred from a Combined U-Pb, Rb-Sr, and Sm-Nd Isotopic Study of the Martian Meteorite Zagami. *Geochimica et Cosmochimica Acta* 69: 5819–30. https://doi.org/10.1016/j.gca.2005.08.007.

Bouvier, A., Blichert-Toft, J., and Albarède, F. 2009. Martian Meteorite Chronology and the Evolution of the Interior of Mars. *Earth and Planetary Science Letters* 280: 285–95. https://doi.org/10.1016/j.epsl.2009.01.042.

Bouvier, A., Blichert-Toft, J., Vervoort, J., and Albarede, F. 2005. The Age of SNC Meteorites and the Antiquity of the Martian Surface. *Earth and Planetary Science Letters* 240: 221–33. https://doi.org/10.1016/j.epsl.2005.09.007.

Bouvier, A., Blichert-Toft, J., Vervoort, J. D., Gillet, P., and Albarède, F. 2008. The Case for Old Basaltic Shergottites. *Earth and Planetary Science Letters* 266: 105–24. https://doi.org/10.1016/j.epsl.2007.11.006.

Britvin, S. N., Krivovichev, S. V., and Armbruster, T. 2016. Ferromerrillite, $Ca9NaFe^{2+}(PO4)7$, a New Mineral from the Martian Meteorites, and Some Insights into Merrillite–Tuite Transformation in Shergottites. *European Journal of Mineralogy* 28: 125–36. https://doi.org/10.1127/ejm/2015/0027-2508.

Carter, J., and Poulet, F. 2013. Ancient Plutonic Processes on Mars Inferred from the Detection of Possible Anorthositic Terrains. *Nature Geosciences* 6: 1008–12. https://doi.org/10.1038/ngeo1995.

Chen, J., Jolliff, B. L., Wang, A., Korotev, R. L., Wang, K., Carpenter, P. K., Chen, H., et al. 2019. Petrogenesis and Shock Metamorphism of Basaltic Lunar Meteorites

Northwest Africa 4734 and 10597. *Journal of Geophysical Research Planets* 124: 2583–98. https://doi.org/10.1029/2019JE006084.

Chen, M., Wopenka, B., Xie, X., and El Goresy, A. 1995. A New High Pressure Polymorph of Chlorapatite in the Shocked Sixiangkou (L6)Chondrite (Abstract). 26th Lunar and Planetary Science Conference. pp. 237–8.

Combs, L. M., Udry, A., Howarth, G. H., Righter, M., Lapen, T. J., Gross, J., Ross, D. K., Rahib, R. R., and Day, J. M. D. 2019. Petrology of the Enriched Poikilitic Shergottite Northwest Africa 10169: Insight into the Martian Interior. *Geochimica et Cosmochimica Acta* 266: 435–62. https://doi.org/10.1016/j.gca.2019.07.001.

Cuscó, R., Guitián, F., Aza, S., and Artús, L. 1998. Differentiation Between Hydroxyapatite and β-Tricalcium Phosphate by Means of μ-Raman Spectroscopy. *Journal of the European Ceramic Society* 18: 1301–5. https://doi.org/10.1016/S0955-2219(98)00057-0.

Deer, W. A., Howie, R. A., and Zussman, J. 2013. *An Introduction to the Rock-Forming Minerals*. 3rd edition. London: Mineralogical Society of Great Britain and Ireland.

El Goresy, A., Gillet, P., Miyahara, M., Ohtani, E., Ozawa, S., Beck, P., and Montagnac, G. 2013. Shock-Induced Deformation of Shergottites: Shock-Pressures and Perturbations of Magmatic Ages on Mars. *Geochimica et Cosmochimica Acta* 101: 233–62. https://doi.org/10.1016/j.gca.2012.10.002.

El Goresy, A., Ramdohr, P., Medenbach, O., and Bernhardt, H.-J. 1974. Taurus-Littrow Crystalline Rocks: Opaque Mineralogy and Geochemistry (Abstract). Fifth Lunar Science Conference. pp. 209–11.

El Goresy, A., Taylor, L. A., and Ramdohr, P. 1972. Fra Mauro Crystalline Rocks: Mineralogy, Geochemistry, and Subsolidus Reduction of the Opaque Minerals. Proceedings, 3rd Lunar Science Conference. p. 333.

Ferdous, J., Brandon, A. D., Peslier, A. H., and Pirotte, Z. 2017. Evaluating Crustal Contributions to Enriched Shergottites from the Petrology, Trace Elements, and Rb-Sr and Sm-Nd Isotope Systematics of Northwest Africa 856. *Geochimica et Cosmochimica Acta* 211: 280–306. https://doi.org/10.1016/j.gca.2017.05.032.

Filiberto, J., Gross, J., Trela, J., and Ferre, E. C. 2014. Gabbroic Shergottite Northwest Africa 6963: An Intrusive Sample of Mars. *American Mineralogist* 99: 601–6. https://doi.org/10.2138/am.2014.4638.

Filiberto, J., Gross, J., Udry, A., Trela, J., Wittmann, A., Cannon, K. M., Penniston-Dorland, S., et al. 2018. Shergottite Northwest Africa 6963: A Pyroxene-Cumulate Martian Gabbro. *Journal of Geophysical Research: Planets* 123: 1823–41. https://doi.org/10.1029/2018JE005635.

Fritz, J., Greshake, A., and Fernandes, V. A. 2017. Revising the Shock Classification of Meteorites. *Meteoritics & Planetary Science* 52: 1216–32. https://doi.org/10.1111/maps.12845.

Gain, S. E. M., Gréau, Y., Henry, H., Belousova, E., Dainis, I., Griffin, W. L., and O'Reilly, S. Y. 2019. Mud Tank Zircon: Long-Term Evaluation of a Reference Material for U-Pb Dating, Hf-Isotope Analysis and Trace Element Analysis. *Geostandards & Geoanalytical Research* 43: 339–54. https://doi.org/10.1111/ggr.12265.

Gancarz, A., Albee, A., and Chodos, A. 1972. Comparative Petrology of Apollo 16 Sample 68415 and Apollo 14 Samples 14276 and 14310. *Earth and Planetary Science Letters* 16: 307–30. https://doi.org/10.1016/0012-821X(72)90150-1.

Gatehouse, B. M., Grey, I. E., Lovering, J. F., and Wark, D. A. 1977. Structural Studies on Tranquillityite and Related Synthetic Phases. Proceedings, 8th Lunar Science Conference. pp. 1831–8.

Gattacceca, J., McCubbin, F. M., Grossman, J., Bouvier, A., Bullock, E., Chennaoui Aoudjehane, H., Debaille, V., et al. 2021. The Meteoritical Bulletin, No. 109. *Meteoritics & Planetary Science* 56: 1626–30. https://doi.org/10.1111/maps.13714.

Gerdes, A., and Zeh, A. 2006. Combined U–Pb and Hf Isotope LA-(MC-)ICP-MS Analyses of Detrital Zircons: Comparison with SHRIMP and New Constraints for the Provenance and Age of an Armorican Metasediment in Central Germany. *Earth and Planetary Science Letters* 249: 47–61. https://doi.org/10.1016/j.epsl.2006.06.039.

Gerdes, A., and Zeh, A. 2009. Zircon Formation Versus Zircon Alteration—New Insights from Combined U–Pb and Lu–Hf In-Situ LA-ICP-MS Analyses, and Consequences for the Interpretation of Archean Zircon from the Central Zone of the Limpopo Belt. *Chemical Geology* 261: 230–43. https://doi.org/10.1016/j.chemgeo.2008.03.005.

Goldoff, B., Webster, J. D., and Harlov, D. E. 2012. Characterization of Fluor-Chlorapatites by Electron Probe Microanalysis with a Focus on Time-Dependent Intensity Variation of Halogens. *American Mineralogist* 97: 1103–15. https://doi.org/10.2138/am.2012.3812.

Goodrich, C. A. 2003. Petrogenesis of Olivine-Phyric Shergottites Sayh al Uhaymir 005 and Elephant Moraine A79001 Lithology A. *Geochimica et Cosmochimica Acta* 67: 3735–72. https://doi.org/10.1016/S0016-7037(03)00171-6.

Gross, J., and Filiberto, J. 2014. Granitic Compositions in Gabbroic Martian Meteorite NWA 6963 and a Possible Connection to Felsic Compositions of the Martian Surface (Abstract #1440). 45th Lunar and Planetary Science Conference. CD-ROM.

Hamilton, V. E., and Filiberto, J. 2015. Crystallinity and Preferred Orientation of Phases in Gabbroic Shergottite NWA 6963 (Abstract #2712). 46th Lunar and Planetary Science Conference. CD-ROM.

Hartmann, W. K., Malin, M., McEwen, A., Carr, M., Soderblom, L., Thomas, P., Danielson, E., James, P., and Veverka, J. 1999. Evidence for Recent Volcanism on Mars from Crater Counts. *Nature* 397: 586–9. https://doi.org/10.1038/17545.

Harvey, R. P., McCoy, T. J., and Leshin, L. A. 1996. Shergottite QUE 94201: Texture, Mineral Compositions, and Comparison with Other Basaltic Shergottites (Abstract #1249). 27th Lunar and Planetary Science Conference. pp. 497–8.

He, Q., Xiao, L., Balta, J. B., Baziotis, I. P., Hsu, W., and Guan, Y. 2015. Petrography and Geochemistry of the Enriched Basaltic Shergottite Northwest Africa 2975. *Meteoritics & Planetary Science* 50: 2024–44. https://doi.org/10.1111/maps.12571.

Herd, C. D., Walton, E. L., Agee, C. B., Muttik, N., Ziegler, K., Shearer, C. K., et al. 2017. The Northwest Africa 8159 Martian Meteorite: Expanding the Martian Sample Suite to the Early Amazonian. *Geochimica et Cosmochimica Acta* 218: 1–26. https://doi.org/10.1016/j.gca.2017.08.037.

Herd, C. D. K., Moser, D. E., Tait, K., Darling, J. R., Shaulis, B. J., McCoy, T. J. 2018. Crystallization of Baddeleyite in Basaltic Rocks from Mars, and Comparisons with the Earth, Moon, and Vesta. In *Microstructural Geochronology*, edited by D. E. Moser, F. Corfu, J. R. Darling, S. M. Reddy, and K. Tait. Hoboken, New Jersey: John Wiley & Sons, Inc (Geophysical Monograph Series). 137–66.

Herd, C. D. K., Simonetti, A., and Peterson, N. D. 2007. In Situ U-Pb Geochronology of Martian Baddeleyite by Laser Ablation MC-ICP-MS (Abstract #1664). 38th Lunar and Planetary Science Conference. CD-ROM.

Herd, C. D. K., Treiman, A. H., Mckay, G. A., and Shearer, C. K. 2004. The Behavior of Li and B During Planetary Basalt Crystallization. *American Mineralogist* 89: 832–40. https://doi.org/10.2138/am-2004-5-618.

Herzog, G. F., and Caffee, M. W. 2014. Cosmic-Ray Exposure Ages of Meteorites. In *Treatise on Geochemistry*, edited by H. D. Holland, 2nd ed., 419–54. Amsterdam: Elsevier.

Hughes, J. M., Jolliff, B. L., and Rakovan, J. 2008. The Crystal Chemistry of Whitlockite and Merrillite and the Dehydrogenation of Whitlockite to Merrillite. *American Mineralogist* 93: 1300–5. https://doi.org/10.2138/am.2008.2683.

Humayun, M., Nemchin, A., Zanda, B., Hewins, R. H., Grange, M., Kennedy, A., Lorand, J. P., et al. 2013. Origin and Age of the Earliest Martian Crust from Meteorite NWA 7533. *Nature* 503: 513–6. https://doi.org/10.1038/nature12764.

Ikeda, Y. 2005. Magmatic Inclusions in Martian Meteorites. *Antarctic Meteorite Research* 18: 170–87.

Jolliff, B. L., Haskin, L. A., Colson, R. O., and Wadhwa, M. 1993. Partitioning in REE-Saturating Minerals: Theory, Experiment, and Modelling of Whitlockite, Apatite, and Evolution of Lunar Residual Magmas. *Geochimica et Cosmochimica Acta* 57: 4069–94. https://doi.org/10.1016/0016-7037(93)90354-Y.

Jolliff, B. L., Hughes, J. M., Freeman, J. J., and Zeigler, R. A. 2006. Crystal Chemistry of Lunar Merrillite and Comparison to Other Meteoritic and Planetary Suites of Whitlockite and Merrillite. *American Mineralogist* 91: 1583–95. https://doi.org/10.2138/am.2006.2185.

Knapmeyer-Endrun, B., Panning, M. P., Bissig, F., Joshi, R., Khan, A., Kim, D., Lekić, V., et al. 2021. Thickness and Structure of the Martian Crust from InSight Seismic Data. *Science* 373: 438–43. https://doi.org/10.1126/science.abf8966.

Koike, M., Ota, Y., Sano, Y., Takahata, N., and Sugiura, N. 2014. High-Spatial Resolution U-Pb Dating of Phosphate Minerals in Martian Meteorite Allan Hills 84001. *Geochemical Journal* 48: 423–31. https://doi.org/10.2343/geochemj.2.0319.

Koike, M., Sano, Y., Takahata, N., Ishida, A., Sugiura, N., and Anand, M. 2016. Combined Investigation of H Isotopic Compositions and U-Pb Chronology of Young Martian Meteorite Larkman Nunatak 06319. *Geochemical Journal* 50: 363–77. https://doi.org/10.2343/geochemj.2.0424.

Lafuente, B., Downs, R. T., Yang, H., and Stone, N. 2016. 1. The Power of Databases: The RRUFF Project. In *Highlights in Mineralogical Crystallography*, edited by T. Armbruster, and R. M. Danisi, 1–30. Berlin: Walter de Gruyter GmbH.

Lapen, T. J., Righter, M., Andreasen, R., Irving, A. J., Satkoski, A. M., Beard, B. L., Nishiizumi, K., Jull, A. J. T., and Caffee, M. W. 2017. Two Billion Years of Magmatism Recorded from a Single Mars Meteorite Ejection Site. *Science Advances* 3: e1600922. https://doi.org/10.1126/sciadv.1600922.

Leroux, H., and Cordier, P. 2006. Magmatic Cristobalite and Quartz in the NWA 856 Martian Meteorite. *Meteoritics & Planetary Science* 41: 913–23. https://doi.org/10.1111/j.1945-5100.2006.tb00495.x.

Li, Q.-L., Zhou, Q., Liu, Y., Xiao, Z., Lin, Y., Li, J.-H., Ma, H. X., et al. 2021. Two-Billion-Year-Old Volcanism on the Moon from Chang'e-5 Basalts. *Nature* 600: 54–8. https://doi.org/10.1038/s41586-021-04100-2.

Lindner, M., Schmitt, A. K., Krot, A. N., and Brenker, F. E. 2020. Rhyolitic (Micrographic Granite) Igneous Clast from Ancient Mars in Meteorite Northwest Africa 8171 (Abstract #1382). 51st Lunar and Planetary Science Conference. CD-ROM.

Lovering, J. F., Wark, D. A., Reid, A. F., Ware, N. G., Keil, K., Prinz, M., et al. 1971. Tranquillityite: A New Silicate Mineral from Apollo 11 and Apollo 12 Basaltic Rocks. Proceedings, 2nd Lunar Science Conference. pp. 39–45.

Ludwig, K. R. 1998. On the Treatment of Concordant Uranium-Lead Ages. *Geochimica et Cosmochimica Acta* 62: 665–76. https://doi.org/10.1016/S0016-7037(98)00059-3.

Marks, E., Gaffney, A. M., and DePaolo, D. 2010. The Relationship of Northwest Africa 4468 to the Other Incompatible-Element-Enriched Shergottites Inferred from Its Rb-Sr and Sm-Nd Isotopic Systematics (Abstract #2064). 41st Lunar and Planetary Science Conference. CD-ROM.

McFarlane, C. R., and Spray, J. G. 2022. The Los Angeles Martian Diabase: Phosphate U-Th-Pb Geochronology and Mantle Source Constraints. *Geochimica et Cosmochimica Acta* 326: 166–79. https://doi.org/10.1016/j.gca.2022.04.006.

McSween, H. Y. 2015. Petrology on Mars. *American Mineralogist* 100: 2380–95. https://doi.org/10.2138/am-2015-5257.

McSween, H. Y., Eisenhour, D. D., Taylor, L. A., Wadhwa, M., and Crozaz, G. 1996. QUE94201 Shergottite: Crystallization of a Martian Basaltic Magma. *Geochimica et Cosmochimica Acta* 60: 4563–9. https://doi.org/10.1016/S0016-7037(96)00265-7.

Meyer, H. O. A., and Boctor, N. Z. 1974. Opaque Mineralogy: Apollo 17, Rock 75035. Proceedings, 5th Lunar Science Conference. (Supplement 5, Geochemica et Cosmochemica Acta). pp. 707–16.

Moser, D. E., Chamberlain, K. R., Tait, K. T., Schmitt, A. K., Darling, J. R., Barker, I. R., and Hyde, B. C. 2013. Solving the Martian Meteorite Age Conundrum Using Micro-Baddeleyite and Launch-Generated Zircon. *Nature* 499: 454–7. https://doi.org/10.1038/nature12341.

Murayama, J. K., Nakai, S., Kato, M., and Kumazawa, M. 1986. A Dense Polymorph of $Ca_3(PO_4)2$: A High Pressure Phase of Apatite Decomposition and its Geochemical Significance. *Physics of the Earth and Planetary Interiors* 44: 293–303. https://doi.org/10.1016/0031-9201(86)90057-9.

Nyquist, L. E., Bogard, D. D., Shih, C.-Y., Greshake, A., Stöffler, D., and Eugster, O. 2001. Ages and Geologic Histories of Martian Meteorites. *Space Science Reviews* 96: 105–64. https://doi.org/10.1023/A:1011993105172.

Paul, A. N., Spikings, R. A., and Gaynor, S. P. 2021. U-Pb ID-TIMS Reference Ages and Initial Pb Isotope Compositions for Durango and Wilberforce Apatites. *Chemical Geology* 586: 120604. https://doi.org/10.1016/j.chemgeo.2021.120604.

Rasmussen, B., Fletcher, I. R., Gregory, C. J., Muhling, J. R., and Suvorova, A. A. 2012. Tranquillityite: The Last Lunar Mineral Comes Down to Earth. *Geology* 40: 83–6. https://doi.org/10.1130/G32525.1.

Rasmussen, B., Fletcher, I. R., and Muhling, J. R. 2008. Pb/Pb Geochronology, Petrography and Chemistry of Zr-Rich Accessory Minerals (Zirconolite, Tranquillityite and Baddeleyite) in Mare Basalt 10047. *Geochimica et Cosmochimica Acta* 72: 5799–818. https://doi.org/10.1016/j.gca.2008.09.010.

Ruzicka, A., Grossman, J. N., and Garvie, L. 2014. The Meteoritical Bulletin, No. 100. *Meteoritics & Planetary Science* 49: E1–E101. https://doi.org/10.1111/maps.12342.

Sautter, V., Toplis, M. J., Wiens, R. C., Cousin, A., Fabre, C., Gasnault, O., Maurice, S., et al. 2015. In Situ Evidence for Continental Crust on Early Mars. *Nature Geoscience* 8: 605–9. https://doi.org/10.1038/ngeo2474.

Schindelin, J., Arganda-Carreras, I., Frise, E., Kaynig, V., Longair, M., Pietzsch, T., Preibisch, S., et al. 2012. Fiji: An Open-Source Platform for Biological-Image Analysis. *Nature Methods* 9: 676–82. https://doi.org/10.1038/nmeth.2019.

Selin, R., Gross, J., and Filiberto, J. 2014. Water, Fluorine, and Chlorine Fugacity Ratios of the Martian Interior Derived from Apatite in Gabbroic Shergottite NWA 6963 (Abstract #1462). 45th Lunar and Planetary Science Conference. CD-ROM.

Shafer, J. T., Brandon, A. D., Lapen, T. J., Righter, M., Peslier, A. H., and Beard, B. L. 2010. Trace Element Systematics and ^{147}Sm–^{143}Nd and ^{176}Lu–^{176}Hf Ages of Larkman Nunatak 06319: Closed-System Fractional Crystallization of an Enriched Shergottite Magma. *Geochimica et Cosmochimica Acta* 74: 7307–28. https://doi.org/10.1016/j.gca.2010.09.009.

Shearer, C. K., Burger, P. V., Papike, J. J., McCubbin, F. M., and Bell, A. S. 2015. Crystal Chemistry of Merrillite from Martian Meteorites: Mineralogical Recorders of Magmatic Processes and Planetary Differentiation. *Meteoritics & Planetary Science* 50: 649–73. https://doi.org/10.1111/maps.12355.

Sheen, A. I., Herd, C. D. K., Hamilton, J., Walton, E. L., and Goodrich, C. 2021. Petrographic Controls on Baddeleyite Occurrence in a Suite of Eight Basaltic Shergottites. *Meteoritics & Planetary Science* 56: 1502–30. https://doi.org/10.1111/maps.13726.

Shih, C.-Y., Nyquist, L. E., and Reese, Y. 2009. Rb-Sr and Sm-Nd Studies of Olivine-Pyhric Shergottites RBT 04262 and LAR 06319: Isotopic Evidence for Relationship to Enriched Basaltic Shergottites. 40th Lunar and Planetary Science Conference. CD-ROM.

Słaby, E., Förster, H.-J., Wirth, R., Wudarska, A., Birski, Ł., and Moszumańska, I. 2017. Validity of the Apatite/Merrillite Relationship in Evaluating the Water Content in the Martian Mantle: Implications from Shergottite Northwest Africa (NWA) 2975. *Geosciences* 7: 99. https://doi.org/10.3390/geosciences7040099.

Stacey, J. S., and Kramers, J. D. 1975. Approximation of Terrestrial Lead Isotope Evolution by a Two-Stage Model. *Earth and Planetary Science Letters* 26: 207–21. https://doi.org/10.1016/0012-821X(75)90088-6.

Staddon, L. G., Darling, J. R., Schwarz, W. H., Stephen, N. R., Schuindt, S., Dunlop, J., and Tait, K. T. 2021. Dating Martian Mafic Crust; Microstructurally Constrained Baddeleyite Geochronology of Enriched Shergottites Northwest Africa (NWA) 7257, NWA 8679 and Zagami. *Geochimica et Cosmochimica Acta* 315: 73–88. https://doi.org/10.1016/j.gca.2021.09.034.

Stolper, E., and McSween, H. Y. 1979. Petrology and Origin of the Shergottite Meteorites. *Geochimica et Cosmochimica Acta* 43: 1475–98. https://doi.org/10.1016/0016-7037(79)90142-X.

Tartèse, R., Anand, M., and Delhaye, T. 2013. NanoSIMS Pb/Pb Dating of Tranquillityite in High-Ti Lunar Basalts: Constraints on Ages and Duration of High-Ti Volcanism on the Moon (Abstract #1274). 44th Lunar and Planetary Science Conference. CD-ROM.

Taylor, L. A., Nazarov, M. A., Shearer, C. K., McSween, H. Y., Cahill, J., Neal, C. R., et al. 2002. Martian Meteorite Dhofar 019: A New Shergottite. *Meteoritics & Planetary Science* 37: 1107–28. https://doi.org/10.1111/j.1945-5100.2002.tb00881.x.

Terada, K., Monde, T., and Sano, Y. 2003. Ion Microprobe U-Th-Pb Dating of Phosphates in Martian Meteorite ALH 84001. *Meteoritics & Planetary Science* 38: 1697–703. https://doi.org/10.1111/j.1945-5100.2003.tb00009.x.

Thompson, R. M., Xie, X., Zhai, S., Downs, R. T., and Yang, H. 2013. A Comparison of the $Ca_3(PO4)_2$ and $CaSiO_3$ Systems, with a New Structure Refinement of Tuite Synthesized at 15 GPa and 1300 C. *American Mineralogist* 98: 1585–92. https://doi.org/10.2138/am.2013.4435.

Udry, A., Howarth, G. H., Herd, C. D. K., Day, J. M. D., Lapen, T. J., and Filiberto, J. 2020. What Martian Meteorites Reveal About the Interior and Surface of Mars. *Journal of Geophysical Research: Planets* 125: e2020JE006523. https://doi.org/10.1029/2020JE006523.

Ulian, G., Valdre, G., Corno, M., and Ugliengo, P. 2013. The Vibrational Features of Hydroxylapatite and Type A Carbonated Apatite: A First Principle Contribution. *American Mineralogist* 98: 752–9. https://doi.org/10.2138/am.2013.4315.

Váci, Z., and Agee, C. 2020. Constraints on Martian Chronology from Meteorites. *Geosciences* 10: 455. https://doi.org/10.3390/geosciences10110455.

Walton, E. L., and Herd, C. D. K. 2007. Localized Shock Melting in Lherzolitic Shergottite Northwest Africa 1950: Comparison with Allan Hills 77005. *Meteoritics & Planetary Science* 42: 63–80. https://doi.org/10.1111/j.1945-5100.2007.tb00218.x.

Walton, E. L., Irving, A. J., Bunch, T. E., and Herd, C. D. K. 2012. Northwest Africa 4797: A Strongly Shocked Ultramafic Poikilitic Shergottite Related to Compositionally Intermediate Martian Meteorites. *Meteoritics & Planetary Science* 47: 1449–74. https://doi.org/10.1111/j.1945-5100.2012.01407.x.

Walton, E. L., and Spray, J. G. 2003. Mineralogy, Microtexture, and Composition of Shock-Induced Melt Pockets in the Los Angeles Basaltic Shergottite. *Meteoritics & Planetary Science* 38: 1865–75. https://doi.org/10.1111/j.1945-5100.2003.tb00020.x.

Wang, A., Kuebler, K., Jolliff, B., and Haskin, L. A. 2004. Mineralogy of a Martian Meteorite as Determined by

Raman Spectroscopy. *International Journal of Raman Spectroscopy* 35: 504–14. https://doi.org/10.1002/jrs.1175.
Wang, S.-Z., Zhang, A.-C., Pang, R.-L., Chen, J.-N., Gu, L.-X., and Wang, R.-C. 2017. Petrogenesis and Shock Metamorphism of the Enriched Lherzolitic Shergottite Northwest Africa 7755. *Meteoritics & Planetary Science* 52: 2437–57. https://doi.org/10.1111/maps.12931
Ward, D., Bischoff, A., Roszjar, J., Berndt, J., and Whitehouse, M. J. 2017. Trace Element Inventory of Meteoritic Ca-Phosphates. *American Mineralogist* 102: 1856–80. https://doi.org/10.2138/am-2017-6056
Wenzel, A., Filiberto, J., Stephen, N., Schwenzer, S. P., and Hammond, S. J. 2021. Constraints on the Petrologic History of Gabbroic Shergottite Northwest Africa 6963 from Pyroxene Zoning Profiles and Electron Backscattered Diffraction. *Meteoritics & Planetary Science* 56: 1744–57. https://doi.org/10.1111/maps.13737.
Wieler, R., Huber, L., Busemann, H., Seiler, S., Leya, I., Maden, C., Masarik, J., et al. 2016. Noble Gases in 18 Martian Meteorites and Angrite Northwest Africa 7812—Exposure Ages, Trapped Gases, and a Re-Evaluation of the Evidence for Solar Cosmic Ray-Produced Neon in Shergottites and Other Achondrites. *Meteoritics & Planetary Science* 51: 407–28. https://doi.org/10.1111/maps.12600.
Wilson, B. J., McFarlane, C. R. M., and Spray, J. G. 2019. Mineralogy and U/Pb Phosphate Dating of the Los Angeles Martian Diabase (Abstract #2952). 50th Lunar and Planetary Science Conference. CD-ROM.
Wilson, N. V., Agee, C. B., and Sharp, Z. D. 2012. New Martian Shergottite NWA 6963 (Abstract #1696). 43rd Lunar and Planetary Science Conference. CD-ROM.
Wray, J. J., Hansen, S. T., Dufek, J., Swayze, G. A., Murchie, S. L., Seelos, F. P., Skok, J. R., Irwin, R. P., III, and Ghiorso, M. S. 2013. Prolonged Magmatic Activity on Mars Inferred from the Detection of Felsic Rocks. *Nature Geoscience* 6: 1013–7. https://doi.org/10.1038/ngeo1994.
Wu, Y., Hus, W., Li, Q.-L., Che, X., and Liao, S. 2021. Heterogeneous Martian Mantle: Evidence from Petrology, Mineral Chemistry, and In Situ U-Pb Chronology of the Basaltic Shergottite Northwest Africa 8653. *Geochimica et Cosmochimica Acta* 309: 352–65. https://doi.org/10.1016/j.gca.2021.05.011
Xie, X., Gu, X., and Chen, M. 2016. An Occurrence of Tuite, γ-Ca 3 (PO 4) 2, Partly Transformed from Ca-Phosphates in the Suizhou Meteorite. *Meteoritics & Planetary Science* 51: 195–202. https://doi.org/10.1111/maps.12577.
Xie, X., Minitti, M. E., Chen, M., Mao, H., Wang, D., Shu, J., and Fei, Y. 2002. Natural High-Pressure Polymorph of Merrillite in the Shock Veins of the Suizhou Meteorite. *Geochimica et Cosmochimica Acta* 66: 2439–44. https://doi.org/10.1016/S0016-7037(02)00833-5.
Xie, X., Minitti, M. E., Chen, M., Mao, H.-K., Wang, D., Shu, J., and Fei, Y. 2004. Tuite, Gamma-Ca3(PO4)2: A New Mineral from the Suizhou L6 Chondrite. *European Journal of Management* 15: 1001–5. https://doi.org/10.1127/0935-1221/2003/0015-1001.
Xie, X., Yang, H., Gu, X., and Downs, R. T. 2015. Chemical Composition and Crystal Structure of Merrillite from the Suizhou Meteorite. *American Mineralogist* 100: 2753–6. https://doi.org/10.2138/am-2015-5488.
Xie, X., Zhai, S., Chen, M., and Yang, H. 2013. Tuite, γ-Ca 3 (PO 4) 2, Formed by Chlorapatite Decomposition in a Shock Vein of the Suizhou L6 Chondrite. *Meteoritics & Planetary Science* 48: 1515–23. https://doi.org/10.1111/maps.12143.
Yoshida, M., Miyahara, M., Suga, H., Yamaguchi, A., Tomioka, N., Sakai, T., Ohfuji, H., et al. 2021. Elucidation of Impact Event Recorded in the Lherzolitic Shergottite NWA 7397. *Meteoritics & Planetary Science* 56: 1729–43. https://doi.org/10.1111/maps.13735.
Zartman, R. E., and Wasserburg, G. 1969. The Isotopic Composition of Lead in Potassium Feldspars from Some 1.0-b.y. Old North American Igneous Rocks. *Geochimica et Cosmochimica Acta* 33: 901–42. https://doi.org/10.1016/0016-7037(69)90104-5.
Zhou, Q., Herd, C. D., Yin, Q.-Z., Li, X.-H., Wu, F.-Y., Li, Q.-L., et al. 2013. Geochronology of the Martian Meteorite Zagami Revealed by U–Pb Ion Probe Dating of Accessory Minerals. *Earth and Planetary Science Letters* 374: 156–63. https://doi.org/10.1016/j.epsl.2013.05.035.

SUPPORTING INFORMATION

Additional supporting information may be found in the online version of this article.

Appendix S1. Supporting information.

Appendix S2. NWA6963_EPMA_measurements.

Appendix S3. NWA6963_Raman_measurements.

Fig. S1. Qualitative EPMA EDX measurements of Cl-apatite intergrown with a merrillite grain.

Fig. S2. Ternary diagram, after Tartèse et al. (2013), showing the composition of NWA 6963 tranquillityite together with literature values.

Fig. S3. BSE images of merrillite grains after U-Pb measurements.

Fig. S4. Representative SEM EDX spectra of minerals in Si-rich mesostasis of NWA 6963.

Fig. S5. BSE and reflected light images of Si-mesostasis, before and after U–Pb measurements.

Fig. S6. Grain sizes of tranquillityite grains measured for U–Pb dating, plotted against measured $^{207}Pb/^{206}Pb$ ratio (no initial Pb correction, values as given in Table S6).

Fig. S7. A-D: Qualitative EPMA WDS and EDX maps of merrillite grains.

Fig. S8. Schematic view of the weighted mean correction factor for elemental fractionation for a mix of feldspar and tranquillityite sampled by one ablation spot. Gray and orange lines show endmember values for feldspar and tranquillityite, respectively.

Fig. S9. Tera–Wasserburg diagram with tranquillityite points corrected using a weighted mean elemental fractionation correction, instead of a constant −5% correction; relative to NIST SRM 614, on measured $^{206}Pb/^{238}U$ as in Fig. 6, Table S6 (see text in supplementary discussion).

Table S1. LA-MC-ICP-MS U-Th-Pb data report.

Table S2. U–Pb data of references for U–Pb LA-MC-ICP-MS measurements.

Table S3. WDS measurement conditions for 10 kV analyses.

Table S4. WDS measurement conditions for 15 kV analyses.

Table S5. U–Pb data of merrillite LA-MC-ICP-MS measurements.

Table S6. U–Pb data of mesostasis mineral LA-MC-ICP-MS measurements.